

“Massively Parallel Nanostructure Assembly Strategies for Sensing and Information Technology”

2013/May/25

Name of Principal Investigators (PI and Co-PIs): Chad A. Mirkin

- e-mail address : chadnano@northwestern.edu
- Institution : Northwestern University
- Mailing Address : Department of Chemistry, 2145 Sheridan Road, Evanston, IL 60208
- Phone : 847-491-2907
- Fax : 847-467-5123

Name of Principal Investigators (PI and Co-PIs): Seunghun Hong

- e-mail address : shong@phya.snu.ac.kr
- Institution : Seoul National University
- Mailing Address : Department of Physics and Astronomy, Seoul National University, Seoul 151-747, Korea
- Phone : 82-2-880-1343
- Fax : 82-2-884-3002

Period of Performance: May/26/2010 – May/25/2013

**Note: NBIT is a collaborative research program with Korean scientists. Therefore, please include in the report your Korean partner's NBIT research results. Please clearly identify the research that was conducted by the Korean team and U.S. team.*

***Also note that AOARD is required to submit the final report to the Defense Technical Information Center (DTIC), which is open to the public.*

Abstract:

Nanoelectronic platforms, bio-detection strategies, and nanostructured materials are capable of addressing a wide range of challenges, including real-time threat monitoring. However, assembling nanomaterials into useful structures is an overarching challenge in the field. This work has focused on the synthesis of new functional materials and the development of high-throughput, facile methods to assemble nanomaterials into useful structures and was carried out as a collaboration between Prof. Chad A. Mirkin (Northwestern University, USA) and Prof. Seunghun Hong (Seoul National University, Korea). Specifically, gapped nanowires (GNW) were identified as candidate materials for synthesis and assembly as they can have programmable nanoscopic dimensions in addition to microscopic leads that facilitate electrical contact and micromanipulation. Throughout the course of this grant, we reported major accomplishments both in the synthesis and assembly of such structures. Synthetically, we report three advances: (1) the development of a method for incorporating semiconducting carbon nanotubes in the gap of segmented nanowires for high sensitivity chemical sensing, (2) the transfer of sub-10 nm nanogap patterns onto functional surfaces such as graphene, and (3) the utilization of biomaterials with GNWs for energy storage and motility assays. By way of progress in the third initiative, we have developed a facile strategy for fabricating and assembling multi-segmented nanowires functionalized with various substances such as carbon nanotubes, polypyrroles and motor

Report Documentation Page		Form Approved OMB No. 0704-0188
Public reporting burden for the collection of information is estimated to average 1 hour per response, including the time for reviewing instructions, searching existing data sources, gathering and maintaining the data needed, and completing and reviewing the collection of information. Send comments regarding this burden estimate or any other aspect of this collection of information, including suggestions for reducing this burden, to Washington Headquarters Services, Directorate for Information Operations and Reports, 1215 Jefferson Davis Highway, Suite 1204, Arlington VA 22202-4302. Respondents should be aware that notwithstanding any other provision of law, no person shall be subject to a penalty for failing to comply with a collection of information if it does not display a currently valid OMB control number.		
1. REPORT DATE 31 MAY 2013	2. REPORT TYPE Final	3. DATES COVERED 26-05-2010 to 25-05-2013
4. TITLE AND SUBTITLE Massively Parallel Nanostructure Assembly Strategies for Sensing and Information Technology (NBIT Phase II)		5a. CONTRACT NUMBER FA23861014065
		5b. GRANT NUMBER
		5c. PROGRAM ELEMENT NUMBER
6. AUTHOR(S) Chad Mirkin		5d. PROJECT NUMBER
		5e. TASK NUMBER
		5f. WORK UNIT NUMBER
7. PERFORMING ORGANIZATION NAME(S) AND ADDRESS(ES) Northwestern University, 2145 Sheridan Road, Evanston, IL, 60208		8. PERFORMING ORGANIZATION REPORT NUMBER N/A
9. SPONSORING/MONITORING AGENCY NAME(S) AND ADDRESS(ES) AOARD, UNIT 45002, APO, AP, 96338-5002		10. SPONSOR/MONITOR'S ACRONYM(S) AOARD
		11. SPONSOR/MONITOR'S REPORT NUMBER(S) AOARD-104065
12. DISTRIBUTION/AVAILABILITY STATEMENT Approved for public release; distribution unlimited		
13. SUPPLEMENTARY NOTES		

14. ABSTRACT

Nanoelectronic platforms, bio-detection strategies, and nanostructured materials are capable of addressing a wide range of challenges, including real-time threat monitoring. However, assembling nanomaterials into useful structures is an overarching challenge in the field. This work has focused on the synthesis of new functional materials and the development of high-throughput, facile methods to assemble nanomaterials into useful structures and was carried out as a collaboration between Prof. Chad A. Mirkin (Northwestern Univ, USA) and Prof. Seunghun Hong (Seoul National Univ, Korea). Specifically, gapped nanowires (GNW) were identified as candidate materials for synthesis and assembly as they can have programmable nanoscopic dimensions in addition to microscopic leads that facilitate electrical contact and micromanipulation. Throughout the course of this grant, we reported major accomplishments both in the synthesis and assembly of such structures. Synthetically, we report three advances: (1) the development of a method for incorporating semiconducting carbon nanotubes in the gap of segmented nanowires for high sensitivity chemical sensing, (2) the transfer of sub-10 nm nanogap patterns onto functional surfaces such as graphene, and (3) the utilization of biomaterials with GNWs for energy storage and motility assays. By way of progress in the third initiative, we have developed a facile strategy for fabricating and assembling multi-segmented nanowires functionalized with various substances such as carbon nanotubes, polypyrroles and motor proteins. Functionalizing carbon nanotube bridged wires with biological receptors allowed fabrication of biosensors that could detect DNA, biotin, and hexanal, an important proof-of-concept that leads one to believe that these structures may one day bear clinical importance. Also, we have developed fabrication methods for synthesizing nano-storage wires (NSWs) that one can use for the real-time release of biochemical molecules upon the application of electrical stimuli. From an assembly perspective, we report on two major advances: (1) the utilization of DNA-mediated assembly to construct nanostructured surfaces, and (2) a capillary mediated approach for the assembly of nanowires in massive arrays. The facile synthetic and assembly techniques discussed herein set the stage for the widespread utilization of advanced nanomaterials for applications in real-time sensing.

15. SUBJECT TERMS

nano materials, nano science and technology, nano technology, Nanobiotechnology

16. SECURITY CLASSIFICATION OF:

16. SECURITY CLASSIFICATION OF:			17. LIMITATION OF ABSTRACT	18. NUMBER OF PAGES	19a. NAME OF RESPONSIBLE PERSON
a. REPORT	b. ABSTRACT	c. THIS PAGE			
unclassified	unclassified	unclassified	Same as Report (SAR)	47	

proteins. Functionalizing carbon nanotube bridged wires with biological receptors allowed fabrication of biosensors that could detect DNA, biotin, and hexanal, an important proof-of-concept that leads one to believe that these structures may one day bear clinical importance. Also, we have developed fabrication methods for synthesizing nano-storage wires (NSWs) that one can use for the real-time release of biochemical molecules upon the application of electrical stimuli. From an assembly perspective, we report on two major advances: (1) the utilization of DNA-mediated assembly to construct nanostructured surfaces, and (2) a capillary mediated approach for the assembly of nanowires in massive arrays. The facile synthetic and assembly techniques discussed herein set the stage for the widespread utilization of advanced nanomaterials for applications in real-time sensing.

Introduction:

Nanotechnology offers the possibility of revolutionizing many fields through the new properties and phenomena that are present at the nanoscale. Two major challenges that influence every aspect of nanoscience are the difficulty of reliably synthesizing complex structures and subsequently assembling them for a desired application. The goals of this research program were to synthesize functional nanodevices and develop facile routes for fabricating two-dimensional templates for the self-assembly of nanoscale structures. Part of the inspiration for this program came from the natural world. Nature uses self-assembly to synthesize many complex structures such as proteins, viruses, and lipid membranes. In the last decade, the field has exploded with interest in trying to understand and mimic self-assembly processes with natural and synthetic building blocks. From such studies, the concept of directed assembly has emerged. With directed assembly, a template is typically used to guide the assembly process, and kinetic as well as thermodynamic structures can be targeted. The templates are often surface patterns that control the individual placement of building blocks and initiate the assembly process while the building blocks typically are nanoscale synthetic or biological materials that have unique and often times useful properties by virtue of their size, shape, and cooperative interactions. Throughout the course of this work, advances were made on both the synthetic and assembly initiatives. In particular, new methodologies were developed for the synthesis of functional gapped nanowires (GNWs) and their assembly into functional architectures. In the remainder of this report, we overview the experimental details and results of the work carried out under this grant. This progress represents the value to be garnered through the combination of top-down and bottom-up fabrication techniques. These advances are expected to provide new directions for the study of fundamental phenomena related to molecular recognition, charge transport, optical coupling, and integration of molecular motors. These results provide a fully integrated toolkit of nano-bio platforms that could be used for the real-time multiplexed detection of chemicals and investigations of fundamental biological processes, for example those related to protein transport dynamics, biological organization, and cellular communication.

1. Experimental

In this section, we review the experimental techniques used in this work. They are divided into subsections according to the principle project to which they relate. In addition, an overview is given to synthetic techniques used in every project, namely the template-based fabrication of gapped nanowires.

1.1 Gapped nanowire synthesis - Mirkin

In a typical on-wire lithography (OWL) experiment, a 400 nm-thick Ag layer is thermally deposited on one side of a porous anodic aluminum oxide (AAO) template that will serve as a working electrode for the subsequent electrodeposition of the materials used to implement the OWL process. For example, additional Ag was electrochemically deposited using a potentiostat (Reference 600, Gamry Instruments Inc.) to create a uniform working electrode for the deposition of the first Au segments. In this process, a platinum (Pt) counter electrode and an Ag/AgCl reference electrode were used for the electrodeposition process. Following this, the desired Au, Ni, and Au segments were electrodeposited in series. Nanowire structures were formed because the AAO template guides the metal to be deposited along the long axis of the pore while maintaining a consistent nanowire diameter. The lengths of the Ni and Au segments were tailored through control over the total amount of charge passed through the electrochemical cell. Following the deposition, the Ag layer was removed with an etching solution consisting of methanol, 30% ammonium hydroxide, and 30% hydrogen peroxide (4:1:1 v/v/v). The AAO template was then dissolved in an aqueous solution of 3 M NaOH and rinsed thoroughly with deionized (DI) water and ethanol. The NWs were then cast on a solid glass substrate (Figure 1e) and a 50 nm thick silica (SiO₂) backing was deposited using plasma-enhanced chemical vapor deposition (PECVD). Following the deposition of the backing layer, the NWs were then detached from the glass substrate via sonication and dispersed in DI water. After a single fabrication process, we were able to obtain $\sim 10^9$ or more nanowires with the electrochemically programmed Au-Ni-Au architecture. To perform electrical measurements, NWs were cast on a SiO₂ substrate, where source and drain metal electrodes were fabricated on each side of the NW via e-beam lithography.

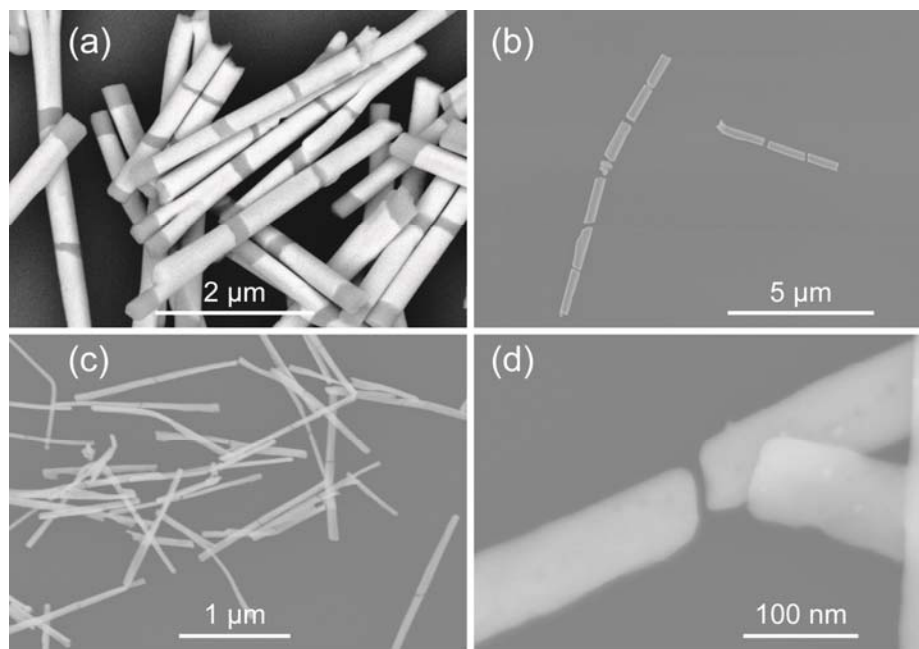


Figure 1. Representative SEM images of gapped nanowires. (a) As-synthesized nanowires with a diameter of 342 ± 34 nm that consists of 3 Au segments of ~ 1.2 μm in length separated by Ni segments of 201 ± 12 and 109 ± 15 nm in length. (b) Examples of gaps formed in the nanowires from (a) after dissolving the Ni segments with HCl. (c) Smaller diameter nanowires (55 nm) with 2 Au segments ~ 750 nm in length separated by a 6 nm Ni segment. (d) A typical sub-10 nm gap in a nanowire formed after removing the Ni segment from one of the wires in (c).

1.2 Synthesis of carbon nanotube-bridge nanowires - Hong

In order to synthesize wires with integrated carbon nanotubes (CNTs), CNTs were assembled on the sidewalls of AAO pores before any electrochemical processing. Because CNTs have a known affinity to Al and Al_2O_3 surfaces, the CNTs were able to assemble onto the sidewalls of the AAO while the aqueous solution containing the surfactant (SDS)-stabilized CNTs is passed through the pores. Nanotube-bridged wire (NBW)-based field effect transistors (FETs) were made by etching the Ni segments in a 1 M aqueous FeCl_3 solution to form CNT channels between the Au segments. The substrate was then washed several times with DI water to remove FeCl_3 , which was followed by further successive rinsing with ethanol and isopropyl alcohol. Finally, isopropyl alcohol was evaporated by a critical point dryer. Finished structures were characterized by SEM, TEM, and energy dispersive X-ray spectroscopy (EDX).

1.3 Nanofabrication of graphene nanoribbons with sub-10 nm gaps - Mirkin

The first step towards creating gapped graphene nanoribbons is to fabricate well-defined metal nanowire etch masks that are secured to a graphene-coated substrate (Figure 2). In a typical experiment, 4-layer graphene (Graphene Supermarket) was coated on a silicon wafer with a 300 nm SiO_2 layer. Multisegmented metal nanowires were synthesized by electrochemically growing alternating Au and Ni segments in an AAO template. The diameter of the nanowires is dictated by the pore size of the AAO template, and in this study,

we utilized both 350 nm and 55 nm diameter nanowires. Prior to depositing the wires on the graphene substrate, the substrate was spin-coated with a thin film (20 nm) of PMMA (495K, Microchem) to serve as an adhesive layer to secure the nanowires and prevent them from migrating during processing. The role of the PMMA is analogous to the role of the silica backing layer in conventional OWL. The nanowires were then drop-cast from an ethanol suspension. Ethanol serves to minimize aggregation of nanowires that can result from the “coffee ring effect”. Strong adhesion between the nanowires and the substrate was achieved by baking the sample on a hot plate at 70 °C for 5 min. Finally, an HCl etch selectively removes the Ni sacrificial segments, thus creating an Au etch mask with a geometry encoded by the electrochemical deposition process used to make the wires.

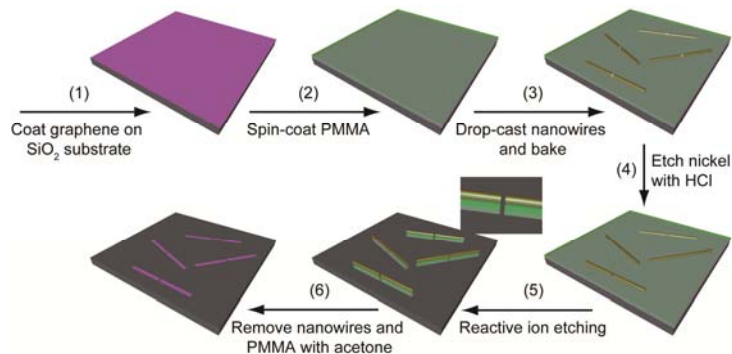


Figure 2. Schematic illustration for making graphene nanoribbons with well-defined gaps using OWL-generated, striped nanowires as etch masks.

Gapped nanowires were used as etch masks in RIE for the fabrication of nanogaps in graphene. For ease of characterization, we began with nanowires defined by 350 nm diameter AAO pores with Ni segments chosen to be 200 and 100 nm. Following synthesis, the average wire diameter is measured to be 342 ± 34 nm with the Ni segments found to be 201 ± 12 and 109 ± 15 nm in average width. In order to achieve anisotropic (or vertical) etching, we chose an etching procedure with literature precedent and optimized gas flow rate, pressure, and power for our system. It was found that the 20 nm PMMA layer was etched in 20 s and 4-layer graphene in another 20 s using a designated set of RIE parameters. After the RIE process, gapped graphene nanoribbons were revealed by using acetone to wash away the PMMA and residual nanowire segments. To further confirm the presence of a gap with no residual graphene, Raman mapping was performed on the as-fabricated nanoribbons. The graphene signal was only observed within the areas protected by the Au segments of the etch mask, and not in the regions below the sacrificial Ni segments.

1.4 DNA-mediated nanoparticle immobilization - Mirkin

The DNA sequences used are outlined in Table 1. The strands were synthesized on a MerMade 48 (MM48) automated oligonucleotide synthesizer (BioAutomation) using standard phosphoramidite chemistry on solid-state supports. The DNA sequences were characterized by matrix-assisted laser desorption ionization time-of-flight mass spectrometry (MALDI-TOF-MS). All molecular weights corresponded to the theoretical mass within the 0.5% resolution limit of the instrument.

Nanoparticle DNA-functionalization was performed using methods described previously. Briefly, the 3' propyl-mercaptan protecting group of the thiolated DNA strand was cleaved in 100 mM dithiothreitol (DTT) (Sigma Aldrich) for 1 h, followed by desalting on a NAP5 size exclusion column (GE Life Sciences). The purified thiolated strands were then added to gold nanoparticles (AuNPs, with a nominal 10 nm diameter) (British Biocell International) in an approximate ratio of 4 nmol per 1 mL nanoparticles. After a several hour incubation period (> 4 h), 2.0 M sodium chloride (NaCl), 1% sodium dodecyl sulfate (SDS) and 1.0 M sodium phosphate (NaPO₄, pH = 7.4) were added stepwise, followed by 10 s sonication, over the course of several hours until a final concentration of 0.5 M NaCl, 10 mM NaPO₄, 0.01% SDS was reached. The solution was then placed on a shaker at ~ 140 RPM overnight to allow for maximum DNA loading. The final spherical nucleic acid (SNA)-AuNPs were then purified by three successive rounds of centrifugation, with each round followed by removal of the supernatant and resuspension in 0.02% aqueous sodium dodecyl sulfate (SDS). After the third round of centrifugation, the SNA-AuNPs were resuspended in 0.5 M phosphate buffered saline (PBS) (10 mM phosphate buffer, 0.5 M NaCl, 0.01% SDS, pH = 7.4). Complementary linker DNA was hybridized to the SNA-AuNPs in a 60:1 molar ratio by slowly cooling through the melting transition from 75 to 45 °C for 30 min followed by heating at 45 °C for 2 h and slowly cooling to room temperature (over ~ 30 min).

Table 1. DNA sequences used in this work.

Description	Sequence
Thiol-modified sequence A	5' AAG AAT TTA TAA GCA GAA - A ₁₀ - (CH ₂) ₃ - SH ^{3'}
Thiol-modified sequence B	5' AAC AAT TAT ACT CAG CAA - A ₁₀ - (CH ₂) ₃ - SH ^{3'}
Linker A	5' TTC TGC TTA TAA ATT CTT - A - TTTCTT ^{3'}
Linker B	5' TTG CTG AGT ATA ATT GTT - A - AAG GAA A ^{3'}

Substrates were functionalized with DNA using a modified procedure as described above. Si wafers (<100>, B doped, 10 Ω-cm - Silicon Quest International, for GISAXS experiments) or quartz slides (Ted Pella, for UV-VIS experiments) were cleaned in boiling piranha (3:1 sulfuric acid, H₂O₂) for 30 - 45 min and rinsed with copious amounts of water (caution! piranha solutions are extremely dangerous and should be handled with care). A thin film of gold (8 nm) was evaporated on the wafers with a 2 nm Cr adhesion layer using a PVD 75 E-beam evaporator (Kurt J. Lesker) at a base pressure of 5×10⁻⁸ torr and evaporation rates of 0.2 Å/s. These conditions yielded a smooth film (RMS roughness < 0.5 nm, as determined by atomic force microscopy) for increased signal-to-noise during x-ray scattering experiments. Additionally, the thin layer of Au was semi-transparent, which allowed for transmission-based UV-VIS measurements. The Au-coated substrates were diced into chips (15 × 7.5 mm²) and functionalized with 2 μM thiolated DNA in 5 mM phosphate buffer, 1 M NaCl for 24 h; note that the mercaptopropyl protecting group on the thiol-modified DNA sequence was cleaved prior to functionalization, as described above. The substrates were then washed 3x in 0.5 M PBS with vigorous agitation to remove unbound DNA. Next, complementary linkers (0.5 μM) were hybridized to the substrates in 0.5 M PBS by heating to 75 °C for 1 min on a heating block, slowly cooling through the melting temperature for 30 min, and heating at 45 °C (~ 10 °C below the melting temperature) for 2 h. The substrates were cooled to room temperature and subsequently washed 3x in 0.5 M PBS. Bi-functionalized DNA substrates were functionalized as described above, except that both

A- and B-type thiol-modified sequences were used for surface functionalization at various ratios (typically 1:1 for (110)-oriented superlattices). After washing, both linkers were hybridized to the substrate at the same molar ratio as the thiol-modified sequences at a total concentration of 0.5 μ M.

1.5 DNA-nanoparticle superlattice growth - Mirkin

SNA superlattices were grown on DNA-substrates using a stepwise approach at temperatures that allowed for simultaneous growth and annealing. In general, substrates and nanoparticles were functionalized with DNA, and complementary linkers that displayed a pendent “sticky end” were subsequently hybridized to these constructs. These DNA-substrates were first immersed in a suspension of A-type SNA-AuNPs, washed, and immersed in B-type SNA-AuNPs. This constituted one “growth-cycle”. Specifically, $15 \times 7.5 \text{ mm}^2$ substrates were immersed in 700 μ L of SNA-AuNPs (5 nM in 0.5 M PBS) in a 2 mL Eppendorf tube, which was

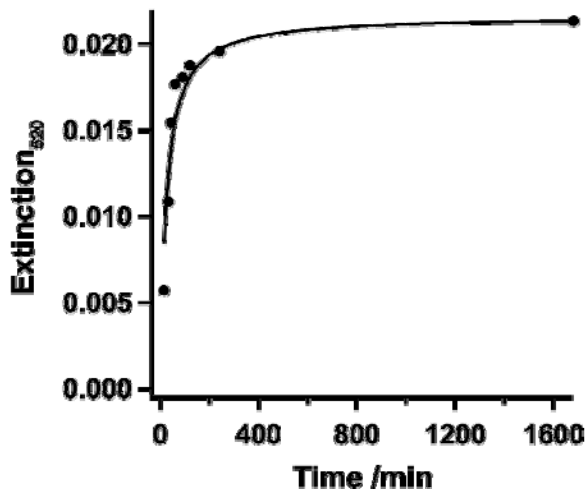


Figure 3. SNA-AuNP binding isotherm to DNA coated substrates at 5 °C below the SNA-AuNP melting temperature.

capped tightly to prevent evaporation. The samples were placed on a heating block (VWR) at various temperatures 0 - 15 °C below the melting temperature. Deposition times were determined from a UV-VIS binding isotherm, which could be fit using second order binding kinetics (Figure 3). Each half-cycle of SNA-AuNPs was deposited for approximately 1 h, which resulted in $\sim 85\%$ of the maximum substrate coverage. No change in GISAXS scattering peak full-width at half-maximum (FWHM) was seen for samples where each half-cycle of SNA-AuNPs was deposited for 2 h, indicating that after 1 h the samples reached their maximally annealed state. Multiple heating blocks were employed to prepare multiple samples at different temperatures simultaneously; the temperature of each heating block was calibrated to an external thermocouple to within 0.1 °C of the nominal temperature, and the variation in temperature was less than 0.15 °C over the entire annealing/growth period. After each half deposition-cycle, the samples were cooled to room temperature, washed carefully in 0.5 M PBS (5x) and immersed in the next SNA-AuNP suspension. This process was repeated until the desired number of half growth-cycles was reached. Once prepared, the samples were stored in 0.5 M PBS at room temperature. No degradation was observed for samples stored in this manner up to 6 months, as determined by GISAXS analysis.

1.6 Silica embedding - Mirkin

In order to remove the nanoparticle thin-film superlattices from the saline environment necessary to preserve Watson-Crick base-pairing and prevent structural collapse, samples were embedded in silica using a sol-gel process. First, 2 μ L of

N-trimethoxysilylpropyl-N,N,N-trimethylammonium chloride (Gelest, 50% in methanol) was added to a thin-film superlattice sample in 1 mL 0.5 M PBS and left to associate with the DNA for 20 min on a rotary shaker (Eppendorf Thermomixer) at 700 RPM at room temperature. Next, 4 μ L triethoxysilane (Sigma Aldrich) was added and the sample was shaken at 700 RPM for 24 h. The samples were then washed in water with vigorous agitation (5 \times) and blown dry with N₂.

1.7 Large-area alignment of multi-segmented metal nanowires – Mirkin and Hong

Multi-segmented nanowires consisting of Au-Ni-Au were electrochemically synthesized in AAO membranes from Synkera Technologies, Inc. having manufacturer-specified pore diameter of 35 nm. The general electrochemical deposition process has been described earlier in this report. Longer nanowires (80 nm Au/20 nm Ni/80 nm Au; nanowire 1) and shorter nanowires 60 nm Au/1-2 nm Ni/60 nm Au; nanowire 2) were synthesized and used for alignment experiments. The synthesized nanowires were functionalized with CTAB in 0.45 mM CTAB aqueous solution (Figure 4A). As shown in Figure 4B (i), a silicon master with positive linelet arrays was made from e-beam lithography using negative-tone resist hydrogensilsesquioxane (HSQ); PDMS stamp (10:1 elastomer to curing agent using SYLGARD® 184 SILICONE ELASTOMER KIT) with negative linelet trenches was made from the master by curing the elastomer precursor at 80 °C for 3 hours. The depth and width of the linelets were 35 nm and 70 nm, respectively. Linelets with a length of 500 nm and 350 nm were used for alignment of nanowires 1 and 2 respectively. A droplet of nanowire solution (in 0.45 mM CTAB) was dropped on the PDMS stamp trench regions and moved over the trenches when it is dried at \sim 40 °C. Figure 4B (ii). The nanowires were aligned to the trenches due to nanoscale capillary force. The aligned nanowires are transferred to either graphene substrate for fabrication of arrays of graphene nanoribbon or 1,4-benzendithiol (1,4-BDT) for SERS study, by micro-contact printing, Figure 4B (iii, iv). PMMA adhesion layer (spin-coated on graphene or 1,4-BDT) and heating at 135 °C facilitate the transfer of nanowires. Arrays of graphene ribbons were fabricated according to the masked etching method described earlier in this report. Raman mapping for SERS was carried out on a Witec instrument using 785 nm laser with a power of 1 mW.

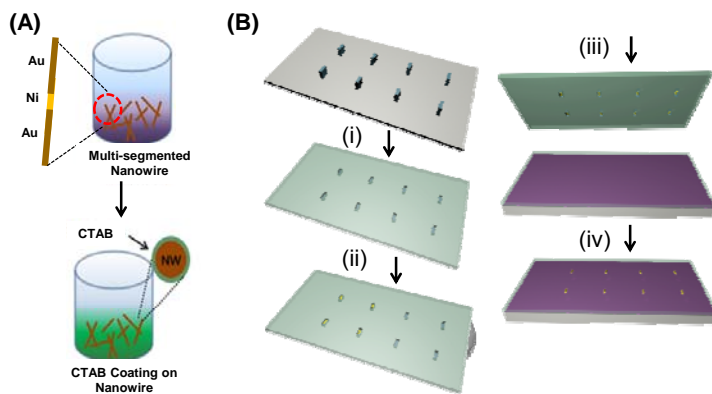


Figure 4. (A) Functionalization of multi-segmented nanowires with CTAB. (B) (i) Fabrication of silicon master with e-beam and PDMS stamp with negative trench linelets. (ii) Alignment of nanowires when nanowire droplet dries and moves over the trench regions in

PDMS stamp. (iii, iv) Transfer of arrays of nanowires to target substrates (graphene or 1,4-BDT) by micro-contact printing.

1.8 Nanotube-bridged wires based biosensors – Mirkin and Hong

Herein, we report the fabrication method used to construct CNT-bridged nanowire-based biosensors. Briefly, nanotube-bridged wires (NBWs) were cast on a solid glass substrate and a 50 nm silicate (SiO_x) film was deposited using PECVD. Following the deposition, the wires were detached from the glass substrate via sonication and dispersed in DI water. After the NBWs were cast on a substrate, source and drain metal electrodes were fabricated on each side of the NBW via e-beam lithography. A NBW-based field effect transistor (FET) was made by etching the Ni segment in a 1 M aqueous FeCl_3 solution to form a semiconducting channel between the Au segments. Finally, a NBW-based biosensor was fabricated by functionalizing NBWs with biological receptors such as membrane protein (receptor 3281) or streptavidin. Receptor 3281 specifically recognizes hexanal that is a biomarker for a lung cancer and streptavidins specifically recognize a type of vitamin called biotin. Through the functionalization of a NBW-based FET sensor with these different biological receptors, we have demonstrated the real-time biosensing of hexanal and biotin.

To fabricate a NBW-based FET biosensor that could detect biotin, we functionalized NBWs with streptavidin. First, a NBW-based FET sensor was immersed in 0.1 M of cysteamine solution for 6 hours in order to functionalize Au segment and Au electrode of the sensor with amine groups ($-\text{NH}_2$). Afterward, the residual cysteamine was removed by immersing the sensor in deionized water for 6 hours. Finally, the sensor was immersed in 1 mg/mL of streptavidin solution for 3 hours to functionalize the NBWs with streptavidin.

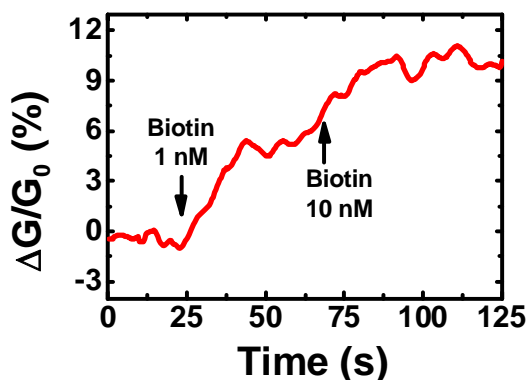


Figure 5. The real-time response of the NBW-based FET functionalized with streptavidin to the injection of 1 nM and 10 nM of biotin solution.

When 1 nM of biotin solution was injected, the sensor showed little increase in the current (5% compared to the initial current). However, when 10 nM of biotin solution was injected, the signal increased by 10%, which was significantly larger than the change induced by the addition of 1 nM of biotin solution (Figure 5).

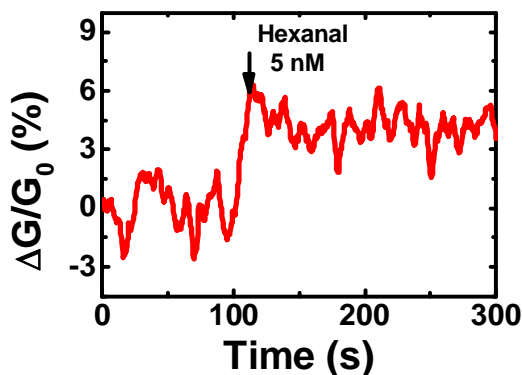


Figure 6. The real-time response of the NBW-based FET functionalized with receptor 3281 to the injection of 5 nM of biotin solution.

To fabricate a NBW-based FET biosensor that could detect hexanal, we functionalized the NBWs with receptor 3281. Here, the NBW-based FET sensor was immersed in 5 mg/mL of receptor 3281 solution for 6 hours in order to functionalize the Au segment and the Au electrode of the sensor with receptor 3281. When 5 nM of hexanal solution was injected, the conductance increased by 5% (Figure 6). Therefore, this result shows that functionalization of a NBWs-based sensor with a suitable biological receptor element allows fabrication of biosensors with high sensitivity.

2. Results and Discussion:

In this section, the major results collected over the course of this grant period are presented and discussed. As in the experimental section, they are divided into subsections according to the principle project to which they relate. All projects advance the principle goal of developing new techniques to synthesize and assemble function nanostructures. Following the reporting of synthetic advances resulting in new electronically functional device architectures, we will report on the new techniques developed to assemble these structures into useful rationally designed architectures.

2.1 Nanofabrication of graphene nanoribbons with sub-10 nm gaps - Mirkin

Graphene nanogaps hold particular promise for a variety of applications in electronics, including their use as atomic scale switches, biomolecular sensors, and the rapid sequencing of DNA. Despite such widespread interest, the lack of reproducible control over gap size with requisite precision makes it difficult to realize this potential. Additionally, such control is important for understanding the fundamental underpinnings of electron transport in gap-based devices, and from a technological standpoint, may open avenues to new types of devices with important applications in molecular electronics, biosensing, and plasmonics. In this regard, it is important to develop reliable methods for introducing sub-10 nm gaps in graphene with control over gap size and position. Thus far, few methods have been developed and implemented for preparing graphene structures with sub-10 nm features. The most popular ones involve drilling with focused electron or ion beams, which are limited by their serial nature. Alternatively, electrical breakdown techniques have been employed, but they suffer

from irreproducibility. Recently, OWL emerged as a method for synthesizing solution-dispersible gapped nanowires with exquisite control over gap length.

Herein, we report a novel method for preparing graphene nanoribbons with sub-10 nm gaps by using etch masks consisting of gapped nanowires generated through the principles of OWL. In this method, nanowires with alternating segments of Ni and Au were electrochemically grown and deposited onto a graphene substrate. The Ni segments were selectively etched with HCl, and then reactive ion etching (RIE) was used to remove the exposed graphene. This process resulted in graphene nanoribbons defined by the Au segments with gaps defined by the original Ni segments. The precision of this approach allows one to control the dimensions of the graphene nanoribbon, in addition to the number, location, and size of the nanogaps (as small as 6 nm) along the ribbon structure.

Having demonstrated the successful preparation of large gaps in graphene nanoribbons, we investigated the potential of this technique for preparing sub-10 nm gaps using narrow nanowires (55 nm diameter) with Ni segments as small as 6 nm (Figure 7). Using the same etching parameters as the larger nanowires, we were able to prepare nanoribbons with 6 nm gaps, demonstrating reliable pattern transfer between the wire and the substrate. As with the larger structures, the graphene nanogap size is in excellent agreement with the length of Ni segments in the nanowires. Electrical characterization was also used to evaluate the electrical properties of graphene nanoribbons. The sheet resistance of a 1 μm long, 35 nm wide continuous graphene ribbon was found to be $470\ \Omega\ \text{Y}^{-1}$, in agreement with reported values. Current-voltage measurements on a ribbon with a 6 nm gap show an open circuit current at voltages up to 35 V, providing further evidence of gap formation.

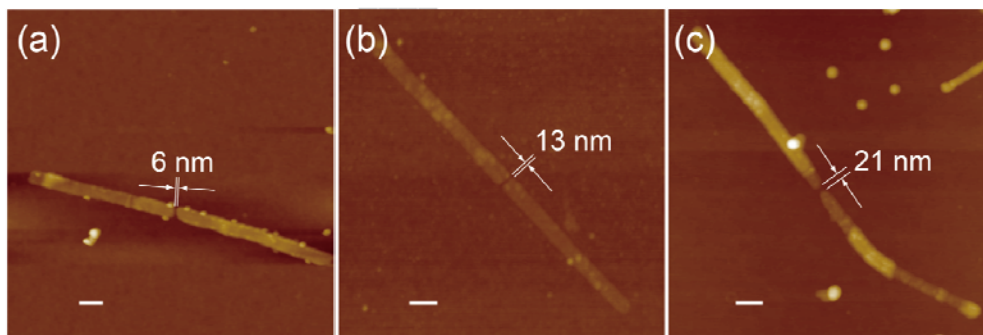


Figure 7. AFM images of smaller nanogaps in graphene nanoribbons, generated by using the structures from Figure 2d as etch masks. (a) A 6 nm gap (RIE time: 40 s). (b) A 13 nm gap (RIE time: 50 s). (c) A 21 nm gap (RIE time: 60 s). Scale bar: 100 nm. The bumps on the graphene are presumed to be residual PMMA, and multi-layer characteristics of CVD-grown graphene manifests as plateaus in the ribbon.

Interestingly, this OWL-based masking approach is quite general and can be used to prepare gapped silicon nanostructures. To make such structures, 55 nm diameter Au-Ni-Au striped wires were deposited onto a silicon-on-insulator wafer (Soitec USA) consisting of a 70 nm thick silicon layer on a 145 nm thick oxide layer. The previously described process was used to remove the Ni segments and etch the exposed substrate, yielding silicon nanostructures with ~ 20 nm gaps. In the case of graphene nanoribbons, it was possible to prepare structures with 6 nm gaps by employing 6 nm Ni segments. However, since the silicon layer is significantly thicker than the graphene, the smallest gap that could be prepared in these proof-of-concept experiments was 20 nm. This limitation is a consequence of the

undercutting that occurs during the RIE process. This is not an inherent limitation of the masking technique as improved etching conditions have been shown to reduce undercutting in other systems, suggesting that further optimization could lead to smaller gaps and even greater control over gap size.

In summary, we have developed a powerful new method for fabricating graphene nanoribbons with gaps as small as 6 nm and silicon structures with slightly larger gaps. Here, 6 nm gaps in nanorods were used to generate 6 nm gaps in a graphene ribbon. Smaller gaps could in principle be generated through the use of nanorods with thinner gaps. As recently we have demonstrated nanorods with gaps as small as 1 nm, the use of this masking technique with such nanorods could generate gaps of the size of single molecules. The reliability, precision, and simplicity of this technique make it particularly attractive for researchers with limited access to sophisticated nanofabrication instruments. It is important to note that in spite of its simplicity, this technique is a remarkably reliable method for generating sub-10 nm features in graphene and, therefore, may play an important role in rapidly prototyping a wide variety of devices with gapped architectures and elucidating the transport mechanisms important to their function.

2.2 Nanotube-bridge wires – Mirkin and Hong

Carbon nanotubes (CNTs) have been utilized for a wide variety of advanced devices due to their remarkable electronic properties. For certain device applications, it is often advantageous to use a short CNT channel. However, at present, there are a limited number of methods to fabricate CNT devices with sub-10 nm channels. Some of these include procedures based upon conventional nanolithography methods such as e-beam lithography, focused-ion beam (FIB), and angled metal deposition. Unfortunately, all of these methods are low-throughput, and no method exists to mass produce the nanostructured devices incorporating sub-10 nm CNT channels, which ultimately limits the viability of CNT-based devices for wide spread application.

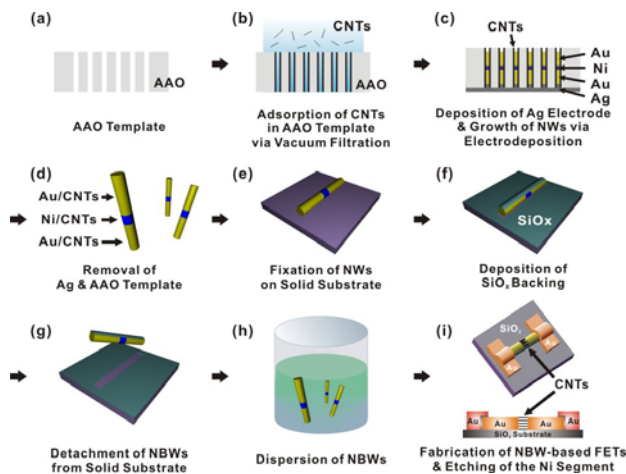


Figure 8. Schematic diagram depicting the fabrication process of NBWs with sub-5-nm-long CNT channels. (a) AAO template. (b) Adsorption of CNTs on the sidewalls of the pores in the AAO template via vacuum filtration. (c) Deposition of Ag electrode and growth of NWs with the segments of Au and Ni via the electrodeposition method. (d) Removal of the AAO template. (e) Fixation of NWs on solid substrate. (f) Deposition of SiO_x backing. (g)

Detachment of the silicate-backed NBWs. (h) Dispersion of the silicate-backed NBWs. (i) Fabrication of NBW-based FETs and etching of the Ni segment.

The fabrication procedure for NBWs is outlined in Figure 8. SEM images of NBWs were taken before (Figure 9a-left) and after (Figure 9a-right) the etching of the Ni segments. The relatively dark area in the middle of the NBW in Figure 9a-left) corresponds to the Ni segment. After removing the Ni segment, the CNTs in the channel region appear to move slightly toward the center of the gap (Figure 9a-right), which is likely due to the absence of the supporting Ni segment. The formation of NBWs with sub-5-nm-long CNT channels were verified by TEM (Figure 9b). Importantly, during the synthesis of these structures, CNTs are likely both on the surface of and embedded within the nanowires. Within one wire, multiple CNT junctions can be fabricated using this novel approach (Figure 9c). For example, in a proof-of-concept experiment, three Ni segments were electrochemically deposited with 1, 2, and 4 coulombs of charge, giving rise to channel lengths of 150, 300, and 600 nm, respectively. This result shows that we can control the number and the length of CNT channels in NBWs simply by controlling the lengths of the Ni segments during the electrodeposition process. Energy dispersive X-ray spectroscopy was subsequently performed to confirm the absence of Ni in the CNT channel. Before chemically etching the Ni segments, two prominent Ni peaks are visible (Figure 9d). After etching with 1M FeCl_3 , these peaks disappear (Figure 9e).

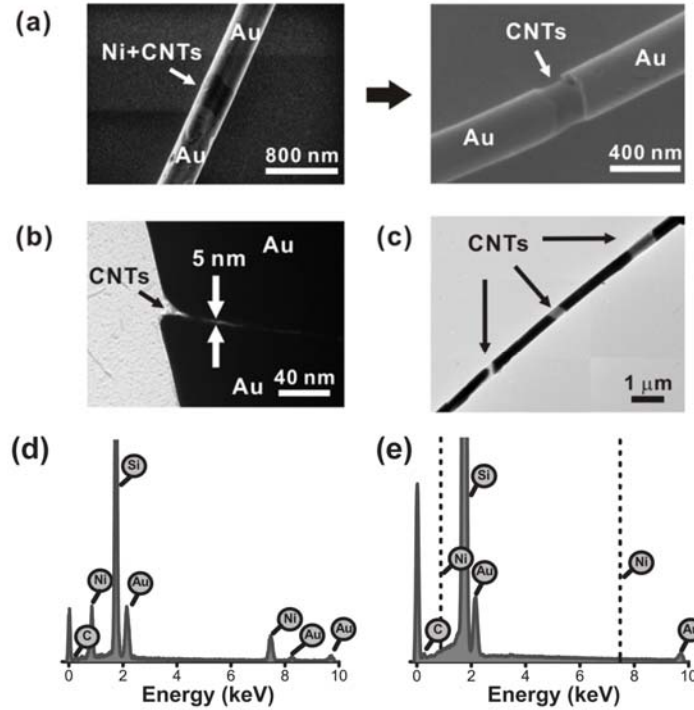


Figure 9. Electron microscopy of NBWs. (a) SEM images of a NBW before (left) and after (right) the removal of the Ni segment. (b) TEM image of a NBW with a 5-nm-long CNT channel. (c) TEM image of a NBW with multiple CNT junctions. Within this image, the four black regions and three grey regions represent Au electrodes and CNT channels, respectively. Two images taken separately are patched to show all three segments in the NBW. (d) EDX spectrum on representative nanowire taken before etching Ni segment. (e) EDX spectrum on

representative nanowire after etching the Ni segments. Their original locations of Ni peaks have been marked by dotted lines for clarity.

Atomic force microscope (AFM)-coupled Raman spectroscopy was used to characterize the NBWs (Figure 10a). In this experiment, Raman spectra were recorded using an AFM-correlated nano-Raman microscope equipped with an inverted optical microscope and a piezoelectric x, y sample scanner manipulated by an independent scanning controller. The 633 nm line of a He-Ne laser was used as the excitation source coupled with a single-mode optical fiber. The tapping-mode closed-loop AFM scanner on top of the closed-loop piezoelectric flexure sample stage was used to correlate the Raman or Rayleigh scattering signal with the AFM topographical image. The laser focal spot was focused on the center of the AFM tip so that it scattered symmetrically off the apex of the AFM tip. The AFM topographical image of the NBWs with a sub-5-nm-long CNT channel (Figure 10a-i) was correlated with the Raman signal (Figure 10a-ii) with an overlap precision of ~ 10 nm. Specifically, the Raman spectrum of a NBW was measured at two different points along the Au wire (P1 and P2) and one channel region (P3). Significantly, G-band and D-band peaks were observed at all three regions (Figure 10a-ii). Note that the G-band and D-band peak intensities at the CNT channel region (P3) were higher than those at the Au electrode regions (P1 and P2). Presumably, the lattice vibration of the CNTs embedded within the Au electrode was inhibited, while that of the CNTs in the channel region was not disturbed because the CNTs were suspended in air after etching the Ni etching.

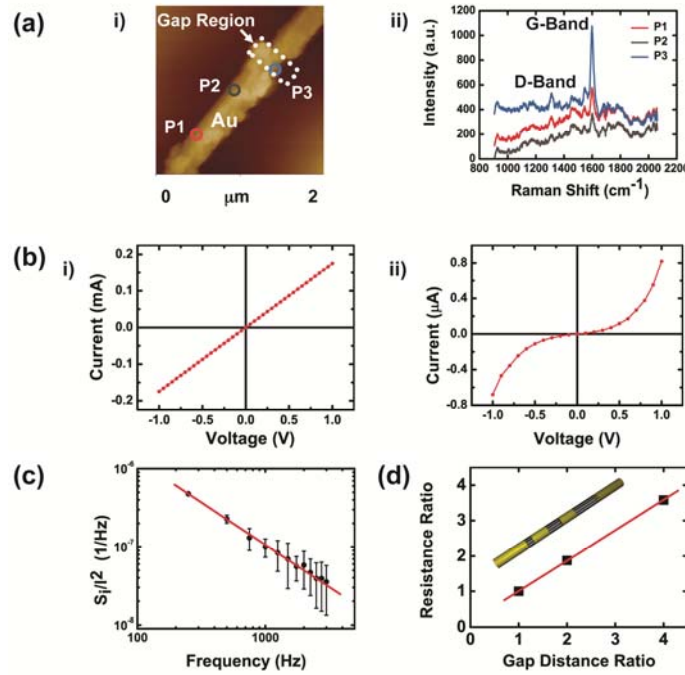


Figure 10. Electronic and optical characterization of NBW-based FETs. (a) AFM-correlated nano-Raman spectroscopic measurements of a NBW. Raman spectroscopy (ii) was performed on the locations of P1, P2, and P3 marked in the AFM image (i) using a 633 nm wavelength laser light with its spot size of 300 nm. (b) IV characteristics of the NBW-based FET i) before and ii) after the removal of the Ni segment. (c) Noise characteristics of the NBW-based FET. The device exhibited a typical $1/f$ noise behavior and a noise-amplitude-to-resistance ratio

$A/R \sim 7.66 \times 10^{-10}$. (d) Graph of the resistance versus gap distance of the NBW-based FET with multiple CNT junctions. The resistance of CNT junctions increased linearly as the gap distance increased and measurements were taken at points along a single nanowire.

The electrical properties of the NBW-based FET were studied before (Figure 10b-i) and after (Figure 10b-ii) Ni etching using a Keithley 4200 semiconductor parametric analyzer. Before removing the Ni segment, the NBW-based FET showed typical Ohmic metallic behavior, however after etching Ni, the device exhibits non-linear IV characteristics, consistent with the formation of the channels with suspended CNTs (compare Figure 10b-I and 10b-ii). The non-linear behavior of the NBW-based FET is due to the formation of a Schottky barrier at the interface between the CNT and Au. Low-bias resistance values were determined for CNT channels of 150, 300, and 600 nm in length respectively, using a two probe method for testing of similar architectures (Figure 10d). A NBW-based FET with the three CNT junctions was fabricated by forming electrodes on each Au segments of the NBW including three CNT junctions via e-beam lithography. The size ratio of the three channels was 1:2:4, which results in a resistance ratio of 1:2:4. Based on these data, one can conclude that these structures exhibit diffusive electrical transport characteristics in agreement with those reported previously.

This novel platform is ideally suited for making and studying CNT-based chemical and biological sensors. As proof-of-concept, a liquid gate profile of a NBW-based FET with a 50-nm channel length was measured to test its response to external electric fields (Figure 11a). The device showed little dependence on the back-gate field, since most of the CNTs in the channel were suspended in air and formed a cylindrical sheet away from the back-gate field. Therefore, we applied a liquid gate bias using a Pt pseudo-reference electrode in 100 μM NaCl solution, while the V_{ds} was kept at 0.1 V. When the gate voltage was swept from -0.4 V to 0.4 V, the device showed an on-off ratio of 2 with a typical hysteresis curve. This dependence shows that the CNT channels in the NBW-based FETs are sensitive to subtle variations in external electric fields. It also suggests that the NBW-based FET can be utilized for chemical sensing.

To test this hypothesis, a NBW-based FET with a 50 nm channel length was synthesized and exposed to NO_2 gas. In this experiment, the resistance of the devices in a gas chamber was monitored at room-temperature while NO_2 gas at different concentrations (0.5, 1, 2, 5, 10 ppm) in N_2 was flowed successively over the device. In agreement with previous reports, the conductance of the CNT channels in the NBW-based FETs increased by the exposure to NO_2 . The response of a NBW-based FET and a planar CNT network-based FET are then compared (Figure 11b). The NBW-based FET current was highly dependent on the exposure to NO_2 gas (Figure 11b-inset). When compared to our results using planar CNT network devices fabricated by the previously-reported surface programmed assembly method, the NBW-based FET with CNT channels exhibited ~ 3 times higher sensitivity. The improved sensitivity of the NBW-based FETs can be attributed, in part, to the increased surface area of the suspended CNTs in the NBW-based FETs. This increase in surface area of CNTs could be advantageous for NO_2 sensing because an increased amount of NO_2 is capable of being absorbed on the exposed surface of the suspended CNTs. Based on these results, it can be concluded that the sensitivity of NBW-based FETs was higher than that of planar CNT-network devices of comparable architecture.

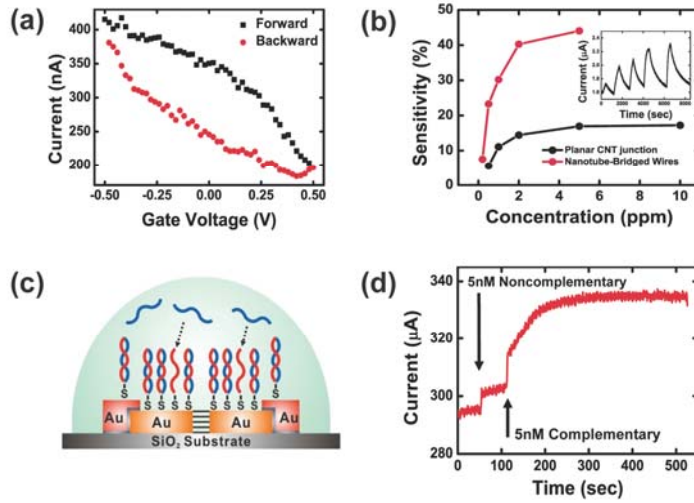


Figure 11. Gating effect measurement and sensing experiment using NBW-based FETs. (a) Liquid gate profile with a typical hysteresis curve. The drain-source voltage was $V_{ds} = 0.1$ V, and a Pt reference electrode was used. (b) Sensitivity dependence on the concentration of NO_2 gas in the NBW-based FET and planar CNT-network devices. The NBW-based FET showed a higher sensitivity than planar CNT-network devices. The inset shows the real-time response of the NBW-based FET to NO_2 gas. (c) Schematic diagram showing the DNA sensing experiment using the NBW-based FET functionalized with thiolated DNA (SH-5'-GCCACAAACACCACAAGA-3') and (d) the real-time response of the NBW-based FET to the injection of non-complementary or complementary DNA molecules.

Finally, we utilize this 50 nm channel length architecture for proof-of-concept real-time DNA sensing (Figure 11c). Here, the Au electrodes in NBW-based FETs were functionalized with the thiolated DNA (SH-5'-GCCACAAACACCA-CAAGA-3') by dipping the NBW-based FETs in the DNA solution (100 nM DNA in DI water) for 6 hours. Then, 10 mM mercaptohexanol was introduced to create adsorbed spacer molecules. Conductance measurements were performed in AC mode (0.5 V_{rms} , 10 kHz) with the DC bias set to 0 V. The signal was amplified with a current gain preamplifier and detected using a lock-in amplifier. Upon injection of 5 nM non-complementary DNA sequences (5'-TGGTGGATCCGT-TCGCTG-3'), the sensor showed little increase in current (Figure 8d). However, when 5 nM complementary DNA sequences (5'-CGGTGTTTGTGGTGTCT-3') were injected, the real-time sensing signal was ~ 5 times higher than that induced by the injection of the non-complementary segments at the same concentration. The rapid conductance increase by injecting complementary DNA segments can be explained by the work function modulation of Au electrodes caused by adsorbed DNA molecules on the electrode. In this case, negatively charged complementary DNA hybridized with the DNA backbone at the electrode surface and induced positive charges on the Au electrodes. This modulation of the work function of the Au electrodes lowered the Schottky barriers between the CNTs and the Au electrodes. The slight conductance increase by injecting non-complementary DNA fragments can be attributed to an increase of the dielectric constant of the solution by the injection. This result shows that our NBWs can be used as a sensing component in biosensors for detecting specific biomolecules.

In summary, we report a simple but efficient method to mass-produce NBWs including CNT channels with channel lengths as small as 5 nm. This method allows one to fabricate NBWs, including single or multiple CNT channels with controlled lengths. Optical

and electrical characterization results show that the CNT channels embedded in the NBW maintain their functionality. Proof-of-concept experiments in the context of chemical and biosensing suggest that they may be useful for such applications, provided adequate levels of sensitivity can be demonstrated, especially with respect to biological analytes.

2.3 Fabrication of multi-segmented conducting polymer nanowires - Hong

Herein, we report simple but efficient method to produce multi-segmented nanowires (MSNs) with polypyrrole segments. The MSNs were synthesized using a modified version of the OWL process. Briefly, a 500 nm-thick silver (Ag) layer was thermally deposited on one side of the AAO template to serve as a working electrode for subsequent electrodeposition. Additional Ag was then electrochemically deposited. Subsequently, Au and polypyrrole (PPy) segments were deposited in series. The Ag backing layer was removed using nitric acid and the AAO was then dissolved in 3M NaOH solution to liberate MSNs.

We have confirmed that the length of the each segment can be controlled by the total amount of charge passing through the electrochemical cell using optical microscopy and SEM.

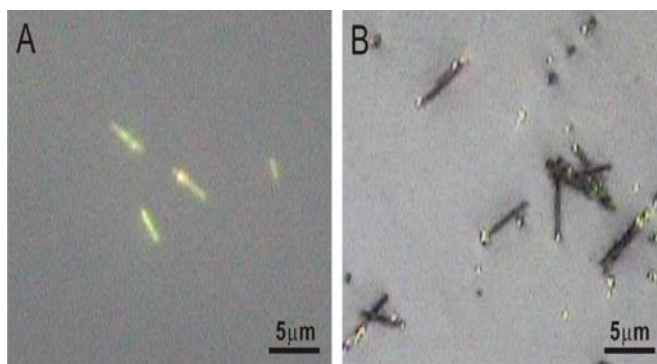


Figure 12. Fluorescence image of MSNs composed of Au (green) and PPy (black) segments. A. MSNs with 10 minutes of PPy deposition. B. MSNs with 1 hour of PPy deposition.

Figure 12A is the optical image of MSNs. Here green region corresponds to gold segment of the MSN, while the black region corresponds to polypyrrole segment, when polypyrrole was deposited for 10 min (Figure 12A), the PPy segment is hardly visible in the fluorescent micrograph. However, when the polypyrrole was deposited for 1 hour, we can confirm that the length of the polypyrrole segment was about 4 μm .

The morphology of MSNs were investigated further using SEM. When the polypyrrole segment was deposited for 10 min, the length of the polypyrrole formed was 100 nm. And the length of PPy segment when the PPy deposition was carried out for 1 hour was 4 μm . This result suggests that the length of the polypyrrole segment in MSNs can be easily controlled by the total amount of charge that has passed through the electrochemical cell.

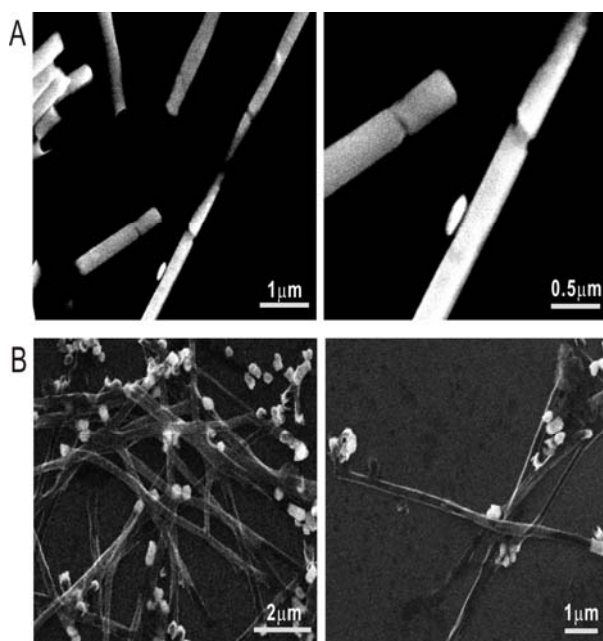


Figure 12. SEM image of MSNs composed of Au (bright) and PPy (black) segments. A. PPy segments of MSNs were deposited for 10 minutes. B. PPy segments of MSNs were deposited for 1 hour.

2.4 Real-time control of biological motor activity using conducting polymers -

Hong

During the deposition of conducting polymers such as polypyrrole, negatively charged chemicals can be incorporated into the polymer matrix. Herein, we have confirmed that incorporated ATP can be released upon an application of bias voltage. First, a photoresist pattern was lithographically defined on a graphene surface, and then PPy-ATP pattern was deposited via electrodeposition. Afterward, a flow cell constructed with double sided tape and Ti/Au (100/300 Å) evaporated cover slide as a spacer and a counter electrode, respectively. A luciferin-luciferase mix stock solution was infused into the flow cell, and then the negative bias voltage (-2 V vs the counter electrode) was repeatedly applied to the flow cell.

We confirmed the release of ATP from PPy-ATP patterns via a bioluminescence assay (Figure 13). The mixture of luciferin and luciferase is often used to monitor the presence of ATP. Luciferin is rapidly oxidized by luciferase in the presence of ATP, producing light. Thus, we can confirm the release of ATP by observing the luminescence from luciferin-luciferase reaction. The luminescence from the reaction was observed via fluorescence microscopy (Figure 13).

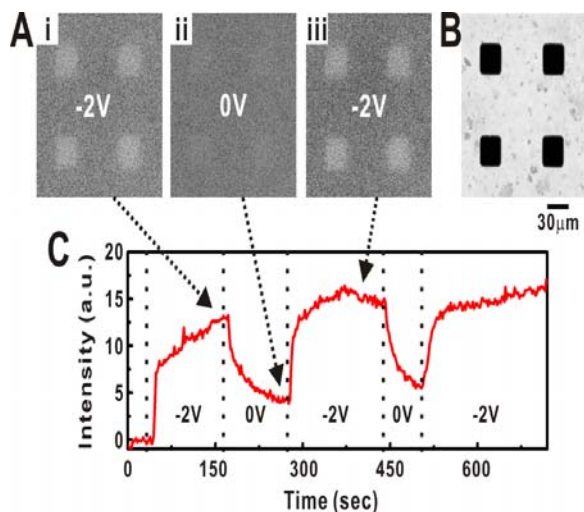


Figure 13. Bioluminescence assay showing the release of ATP from PPy-ATP patterns. A. Luminescence micrographs of a PPy-ATP pattern when -2 V was applied (i,iii) or when the voltage was turned off (ii). B. Optical micrograph of the PPy-ATP patterns (black squares). C. Graph showing the bioluminescence intensity with different bias voltages onto the graphene substrate. The bioluminescence intensity was averaged over four square-shaped PPy-ATP regions. The luminescence intensity indicating ATP molecules was repeatedly increased and decreased by electrical stimuli.

Panels A and B of Figure 13 are the luminescence micrographs at different bias voltages and the optical micrograph of the PPy-ATP patterns, respectively. The four square-shaped dark regions in the optical micrograph (Figure 13B) represent PPy-ATP patterns. The size of the PPy-ATP pattern was $30\ \mu\text{m} \times 30\ \mu\text{m}$, and the space between the patterns was $70\ \mu\text{m}$. When a negative bias voltage of -2 V (vs the counter electrode) was applied, the regions of the PPy-ATP patterns became brighter (Figure 13A (i, iii)). With a zero bias voltage, the luminescence in the PPy-ATP regions faded away (Figure 13A (ii)). This result implies that the incorporated ATP molecules were released from the PPy-ATP patterns with the negative bias voltage, but they were not released after turning off the voltage.

Figure 13C depicts the average luminescence intensity of the four PPy-ATP regions as time passed. The luminescence intensity repeatedly increased or decreased, corresponding with the applied electrical stimuli. This agrees with our hypothesis that ATP molecules were released from the PPy-ATP patterns by the electrical stimuli.

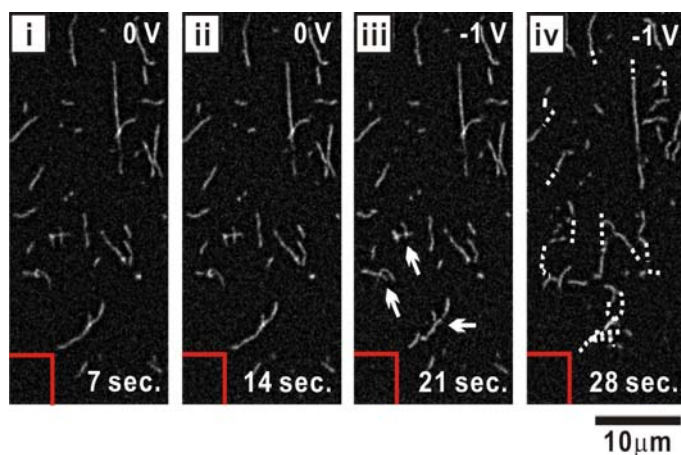


Figure 14. Time series of fluorescence images showing controlled actomyosin motility by electrical stimuli. A PPy-ATP pattern was located in the bottom left of the figure (a red solid line). Note that actin filaments did not move before a voltage was applied (i,ii). (iii) Actin filaments close to a PPy-ATP pattern began to move. The moving actin filaments were indicated by white arrows. (iv) Actin filaments in all regions moved. The trajectories were represented by white dotted lines.

We demonstrated the real-time control of actomyosin motility using the PPy-ATP patterns (Figure 14). Figure 14 depicts a time series of fluorescence micrographs showing the activation of actomyosin by electrical stimuli. A PPy-ATP pattern was located in the bottom left of the figure (a red solid line). Before electrical stimuli, actin filaments on myosin did not move at all because there was no ATP in the buffer solution (Figures 14 i, ii). When a negative bias voltage (-1 V vs the counter electrode) was applied to PPy-ATP patterns through the graphene, the actin filaments began to move (Figures 14iii, iv). The trajectory of actin filaments are represented by white dotted lines in Figure 14iv. The amount of the released ATP by short-time electrical stimuli (20 s) was enough to maintain actomyosin motility over an hour. Interestingly, actin filaments which were close to the PPy-ATP pattern (white arrows in Figure 14iii) began to move first. It implies that the ATP concentration near the PPy-ATP pattern was initially higher than the other region.

2.5 Functionalization of NWs with motor proteins - Hong

In biological systems, bio-motor proteins such as kinesin and myosin deliver cargo to specified locations within a cell by traveling on tracks called cytoskeletons. The ability to control the movement of motors proteins could provide an efficient platform for a micro-/nano-mechanical transport system. Herein, we report a simple but efficient method to produce multi-segmented nanowires functionalized with biomotors. In this system, we have combined OWL with a technique for functionalizing a Au substrate with thiolamine. Combining these technologies has enabled the fabrication of nanowires functionalized with bio-motors molecules called kinesin which then can serve as a guiding track for microtubule movement.

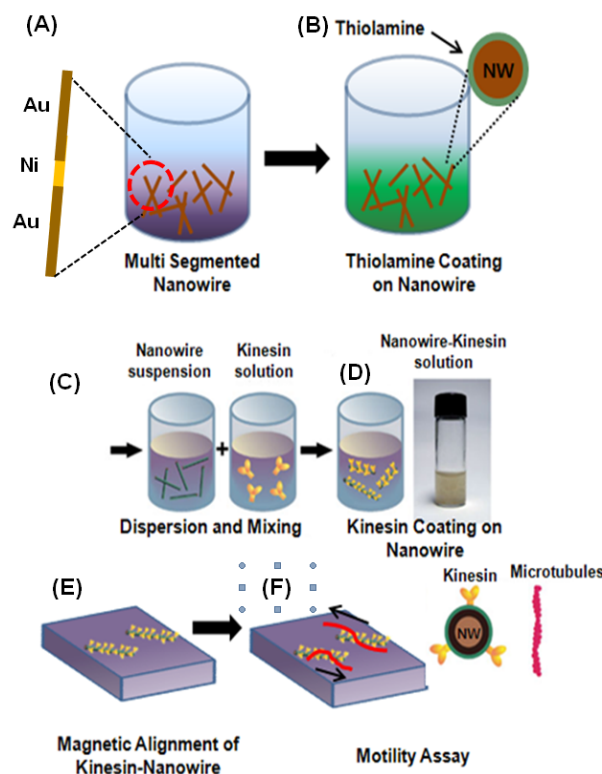


Figure 15. Schematic diagram depicting the fabrication process of multi-segmented nanowires functionalized with kinesin molecules. (A) Multi-segmented nanowire stored in ethanol solution (B) Functionalization of multi-segmented nanowire with thiolamine (C-D) Functionalization of nanowires with kinesin (E) Magnetic alignment of kinesin functionalized nanowires (F) Motility assay of microtubule on kinesin functionalized nanowires.

Multi-segmented nanowires consisting of Au-Ni-Au segments were synthesized using a modified version of the OWL Process (Figure 15A). Afterwards, nanowires were transferred to thiolamine solution for 10 minutes to functionalize them with amine groups ($-\text{NH}_2$) (Figure 15B) and subsequently added kinesin solution to functionalize them with kinesin (Figures 15C-D). Then, the nanowire solution was transferred on to a glass slide and nanowires were aligned via an external magnetic field (Figure 15E). Finally, adenosine triphosphate (ATP) and microtubule solution were added to the aligned nanowires to observe the motility of the bio-motors under fluorescence microscopy (Figure 15F).

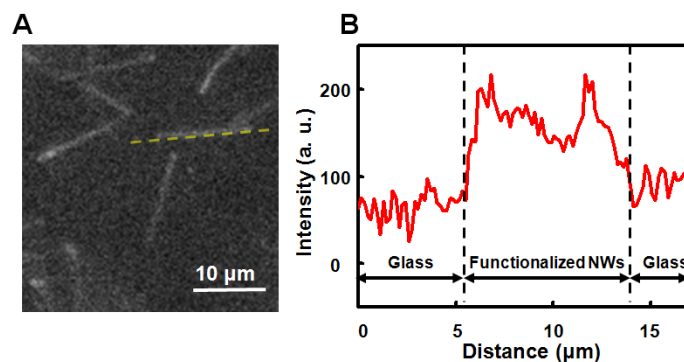


Figure 16. Fluorescence image (A) and intensity profile (B) of multi-segmented nanowires functionalized with kinesin. (B) Intensity profile along the loner axis (yellow dotted line in (A)) of nanowire has been obtained.

Fluorescence microscopy was used to confirm the functionalization of the nanowires with the kinesin molecules. Here, kinesin molecules were fluorescently labeled. It is clear from the fluorescence image that functionalized nanowires are clearly distinguished from glass substrate (Figure 16A) and the intensity profile showed that the fluorescence intensity of the nanowire is up to 3 times higher than the glass slide. This result clearly indicated that only the nanowires are selectively functionalized with kinesin molecules.

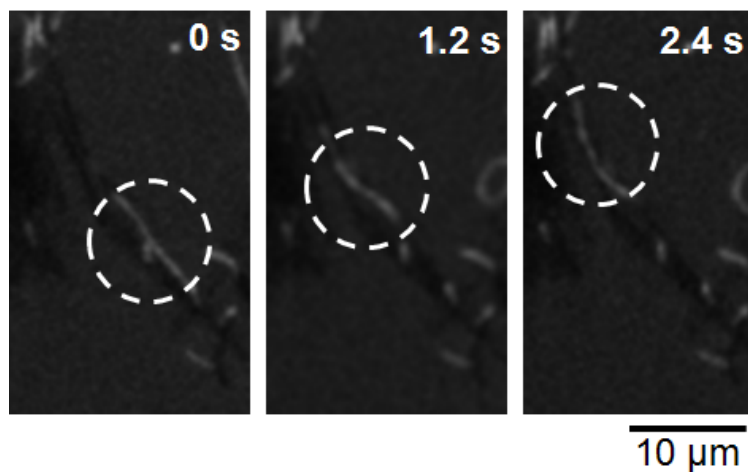


Figure 17. Motility assay of microtubule (bright line) along the kinesin-functionalized nanowires (black line).

Afterwards, the nanowires were aligned using a magnetic field then subjected to a motility assay by adding a solution containing ATP and fluorescently labeled microtubules. We have confirmed that fluorescently labeled microtubules move along the multi-segmented nanowire functionalized with kinesin (Figure 17). The average speed of the microtubules was $4.122 \mu\text{m/s}$. These results show that multi-segmented nanowires functionalized with kinesin can serve as a guiding track for microtubules.

2.6 Printable nano-storage wires - Hong

Most biological reactions that require energy input utilize ATP as an energy currency. Therefore, it is obvious that the development of a device for the controlled release of ATP into the reaction medium grant an ability to control biological reactions at will. Herein, we report a simple but efficient method to mass-produce nano-storage wires (NSWs) with ATP containing conducting polymer segments, which release ATP upon the application of electrical stimuli.

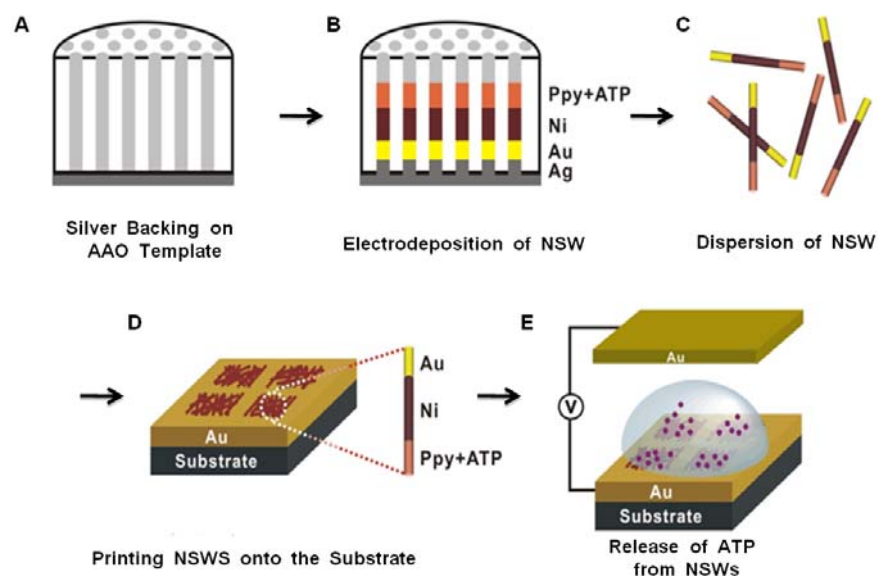


Figure 18. Schematic diagram depicting the fabrication process of nano-storage wires (NSWs) (A) Silver coating on one side of AAO template (B) Electrical deposition of Ag, Au, Ni and PPy-ATP segment in series. (C) Dispersion of NSWs (D) Printing of NSWs on a substrate (E) Release of ATP from NSWs upon electrical stimulus.

The NSWs were synthesized using a modified version of the OWL process. Briefly, a 500 nm-thick silver (Ag) layer was thermally deposited on one side of the AAO template to serve as a working electrode for the succeeding electrodeposition (Figure 18A). Additional Ag was then electrochemically deposited. Subsequently, gold (Au), nickel (Ni) and polypyrrole segments were deposited in series (Figure 18B). Here, the length of the each segment was controlled by the total number of charges passing through the electrochemical cell. The Ag backing layer was removed using nitric acid and the AAO was then dissolved in 3M NaOH solution to liberate the NSWs (Figure 18C). Afterward, NSWs were adhered to a desired substrate via drying NSW solution in vacuum. Finally, electrical stimulus (-3V) was applied to NSWs to release ATP into the solution which in turn can be observed by fluorescence microscopy.

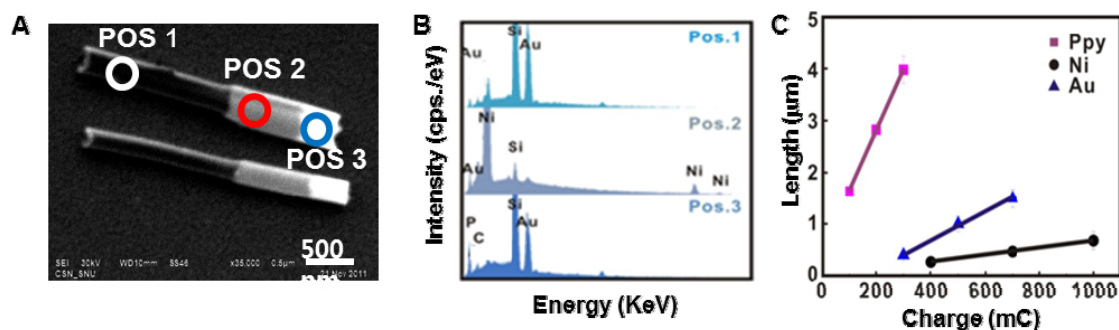


Figure 19. Characterization of NSWs containing ATP (A) Scanning electron microscopy (SEM) image of NSWs composed of three segments, position 1, 2 and 3 represent PPy-ATP, Ni and Au segments, respectively. (B) Energy dispersive X-ray spectroscopy (EDS) data of position 1, 2 and 3. (C) Characterization of the length of each segment versus amount of charges passing through the electrochemical cell.

The scanning electron microscopy (SEM) image of NSWs containing ATP shows three differently contrasting segments indicating the difference in composition (Figure 19A). Energy dispersive X-ray spectroscopy (EDS) was carried out for each segment to identify the composition of each segment (Figure 19B). These measurements showed that position 1 was composed of carbon and phosphate indicating this is the PPy-ATP segment, while position 2 was composed of Ni and position 3 is composed of Au. Characterization of the length of each segment as a function of amount of charge applied indicates that there is a linear relationship between them with a varying degree of dependence for each compound ($0.002 \mu\text{m mC}^{-1}$, $0.014 \mu\text{m mC}^{-1}$ and $0.582 \mu\text{m mC}^{-1}$ for Au, Ni and PPy-ATP respectively).

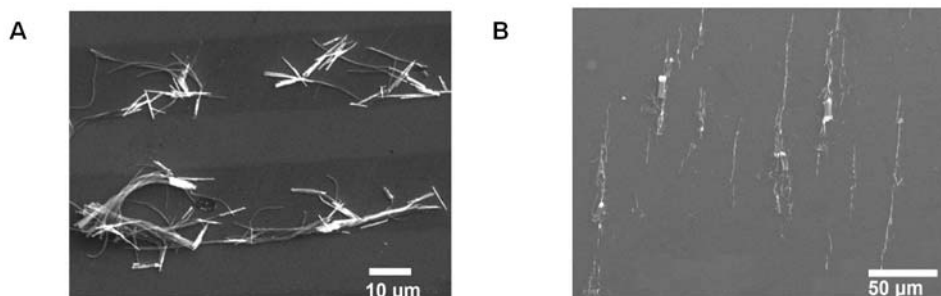


Figure 20. (A) Self-assembly of NSWs in octadecanethiol (ODT) patterns. Bright lines correspond to ODT self-assembled monolayer and dark lines correspond to ODT-free gold substrate. (B) Self-assembly of NSWs via magnetic alignment

NSWs were aligned on octadecanethiol (ODT) patterns (Figure 20A). First, ODT molecules were linearly patterned on to a gold substrate via micro-contact printing followed by drying NSW solution on the substrate. Figure 20A shows that the NSWs are efficiently adhered to ODT-free gold substrate only. Figure 20B shows SEM image of multi-segmented nanowires aligned via magnetic field. Because the NSWs contain a Ni segment, and Ni is intrinsically ferromagnetic, the NSWs become aligned in the presence of an external field. Therefore, the spatial orientation and location NSWs can be controlled.

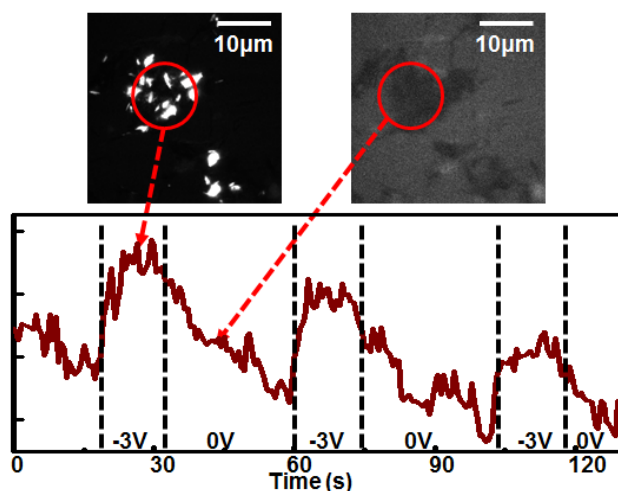


Figure 21. Fluorescence assay of ATP-containing NSWs (A) Fluorescence image of NSWs i) when -3V applied ii) when no voltage was applied (B) Fluorescence intensity profile during series of voltage application.

We confirmed the release of ATP from NSWs via ATP bioluminescence assay kit which is a mixture of luciferin and luciferase. As discussed previously, luciferin is rapidly oxidized by luciferase in the presence of ATP, producing light. Thus, we can confirm the release of ATP by observing the fluorescence from luciferin-luciferase solution. When -3 V was applied to NSWs, they emitted bright light which indicates the release of ATPs. This result coincides with the fluorescence intensity profile graph (Figure 21B) where intensity of the fluorescence image rapidly increased after the voltage application. As soon as the voltage was removed, ATP molecules free in solution start to deplete by luciferase and hence fluorescence starts to diminish. In conclusion, we have demonstrated efficient methods to mass-produce NSWs with ATP containing conducting polymer segments which can release ATP upon electrical stimulus. This bio-energy storage system can enable local activation of proteins such as motor proteins with on/off switching. These results clearly show that NSWs are quite versatile structures allowing us to fabricate nano-storage devices on virtually general substrates for the controlled release of biochemical molecules. Thus, our strategy should provide great opportunities in various areas such as drug delivery systems, biosensors and biochips for the controlled release of chemicals to bio-systems. Further work will involve integration of NSWs with bio-motor functionalized multi-segmented nanowires which would enable us to control the biomotor activity.

2.7 Real-time control of biological motor activity using nano-storage wires - Hong

Herein, we report a simple but efficient method for the real-time control of biological motor activity using nano-storage wires (NSWs). In this system, NSW fabrication method and techniques to functionalize nanowires with biological motor was used to fabricate kinesin functionalized NSWs. We then demonstrate that the activity of biological motors can be controlled in real-time via the application of electrical stimuli.

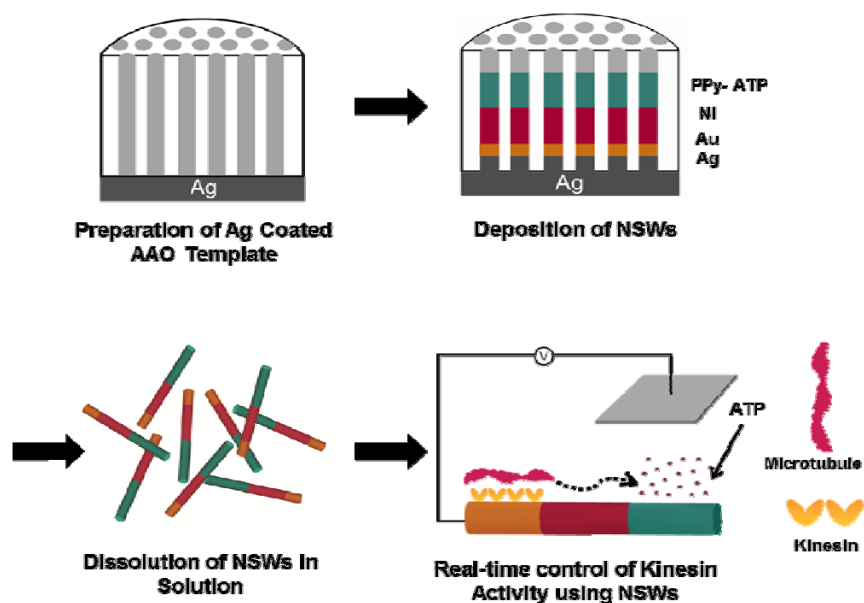


Figure 22. Schematic diagram depicting the fabrication process of nano-storage wires (NSWs) functionalized with biological motors. (A) Silver coating on one side of AAO template (B) Electrical deposition of Ag, Au, Ni and PPy-ATP segment in series. (C) Dispersion of NSWs (D) Functionalization of NSWs with kinsins and release of ATP from NSWs upon electrical stimulus

Briefly, a 500 nm-thick silver (Ag) layer was thermally deposited on one side of the AAO template to serve as a working electrode for the succeeding electrodeposition (Figure 22). Additional Ag was then electrochemically deposited and subsequently, gold (Au), nickel (Ni) and polypyrrole-ATP (PPy-ATP) segments in series. The Ag backing layer was removed using nitric acid and the AAO was then dissolved in 3M NaOH solution to liberate the NSWs. Afterwards, the NSWs were transferred to a cysteamine solution for 10 minutes to functionalize them with amine groups ($-\text{NH}_2$) (Figure 22B). Subsequently, kinesin solution was added to functionalize them with kinesin (Figures 22C, D). Finally, kinesin labeled NSWs were deposited on top of Ti/Au coated glass substrate and the motility of kinesin was controlled via application of -2.5 V.

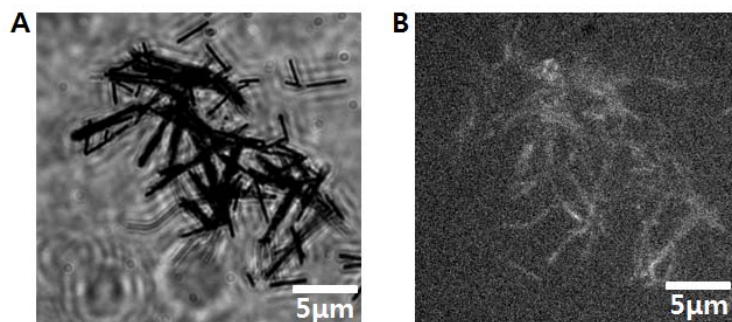


Figure 23. A. Dark field optical and B Fluorescence images of NSWs functionalized with fluorescently labeled kinesin molecules.

We confirmed that the NSWs were functionalized with kinesin using fluorescence microscopy. Here, NSWs were functionalized with fluorescently labeled kinesin molecules. The black lines in the optical image (Figure 23A) and bright lines in the fluorescence image (Figure 23B) correspond to the NSWs. These results clearly indicate that the NSWs were successfully functionalized with kinesin molecules.

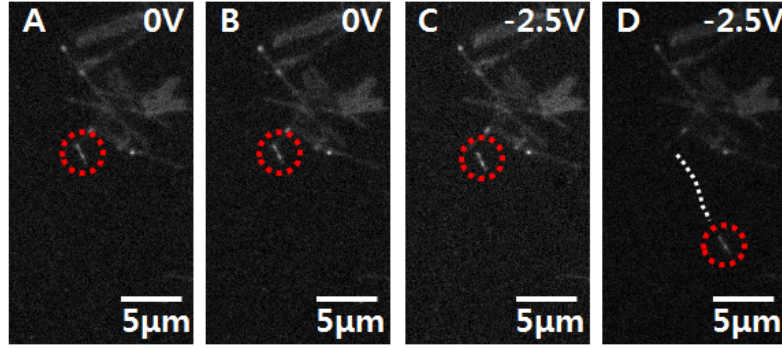


Figure 24. A-B. Fluorescence image of microtubules and NSWs functionalized with kinesin before the application of bias voltage. C-D. Fluorescence image of microtubules and NSWs functionalized with kinesin after the application of bias voltage (-2.5 V).

We have controlled the motility of kinesin molecules via an application of electrical stimuli to the NSWs (Figure 24). Since kinesin requires ATP molecules to generate motion, the released ATP molecules could be utilized to control the activities of kinesin molecules (Figure 24C). Here, NSWs were first deposited onto a thin Au film, and, then, the Au film was utilized as a substrate for the microtubule-kinesin motility assay. The fluorescence image shows the motility of kinesin molecules when electrical stimuli were absent and applied. When there was no applied bias voltages, the microtubules were stationary. However, when a bias voltage was applied onto the substrate, ATP was released from the NSWs. The kinesin molecules were activated, resulting in the motion of microtubules on them. It clearly shows that our NSWs can be utilized to build a device to control protein activities in real time.

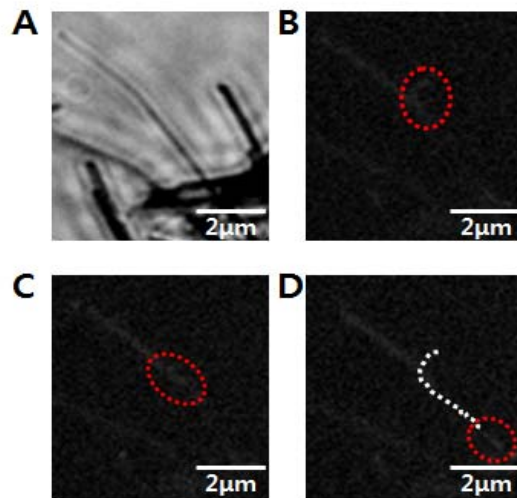


Figure 25. A. Optical image of kinesin functionalized NSWs. B-D. Time series of fluorescence images of kinesin functionalized NSWs and a microtubule (red circle) after the application of bias voltage (-2.5V). The trajectory of the microtubule was represented with white dotted line.

We confirmed that microtubules could glide along the NSWs functionalized with kinesin molecules using fluorescence microscopy. When a bias voltage was applied, ATP molecules were released from the NSWs and hence have activated kinesin molecules attached to the NSWs. Therefore, microtubules start to glide along the NSWs (Figure 25).

In conclusion, we have demonstrated real-time control kinesin molecules that are attached to the NSWs via an application of bias voltages. This strategy allowed local activation of proteins, such as motor proteins. These results clearly show that NSWs provide great opportunities in various areas such as drug delivery systems, biosensors and biochips for the controlled activation of bio-systems.

2.8 Stepwise Evolution of DNA-Programmable Nanoparticle Superlattices - Mirkin

DNA-mediated assembly provides a powerful approach for immobilizing materials on surfaces with a high degree of selectivity and control over interparticle separation. Despite the great interest, and impressive progress in solution-based assembly, DNA-mediated assembly on surfaces has remained a challenge. This is an important area to address as functional devices inevitably must have a rigid support substrate in order to function. Additionally, it would be ideal to be able to lithographically template the assembly of nanoparticles so as to rapidly develop devices that use DNA-immobilized nanoparticles as active elements. Toward this end, we performed a detailed study of DNA-mediated assembly of nanoparticle superlattices on surfaces.

Attractive interactions were mediated with DNA-linkers that displayed hetero-complementary pendent “sticky ends” (Figure 26a). In a typical experiment, superlattices were prepared by successive immersion of the DNA substrate into a suspension of particle “A” and then particle “B” (defined as one growth cycle) at various temperatures (Figure 26a). The samples were characterized by synchrotron grazing incidence small angle

X-ray scattering (GISAXS), a powerful solution-compatible technique that allows one to extract orientation symmetry, lattice parameter, crystallite size and electron density for thin-film superlattices. These data were corroborated with scanning electron microscopy (SEM) of superlattice films embedded in silica.

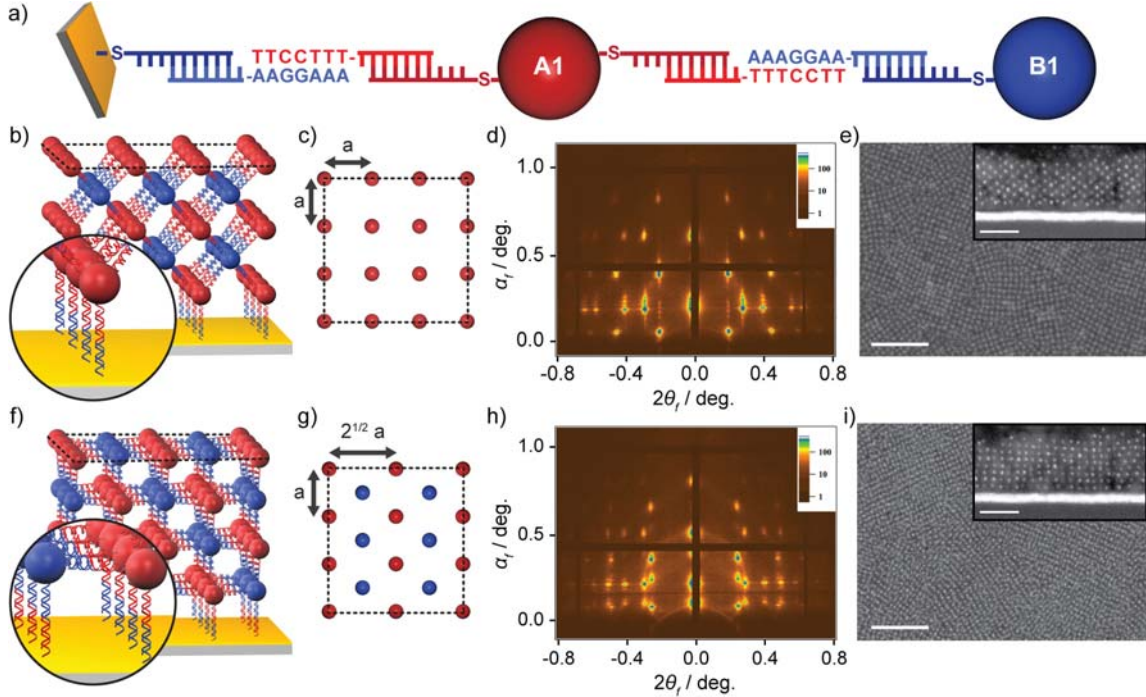


Figure 26. Crystallographic orientation can be programmed by controlling the type of bonding interactions between the superlattice and substrate. a) A binary DNA sequence design enables the stepwise growth of DNA-nanoparticle superlattices with either (100)- (b,c,d,e) or (110)- (f,g,h,i) orientation. Schematic illustrations of (100)- and (110)-oriented bcc superlattices grown on mono- or bi-functionalized substrates, respectively, are shown in (b,f). The (100) orientation formed on substrates that displayed a single type of linker (blue) while the (110) orientation formed on substrates that displayed both types of linkers (blue and red), matching the complementary DNA-functionalized nanoparticles in the (100) (c) and (110) (g) planes. d,e) 2D GISAXS scattering pattern and SEM of (100)-oriented bcc superlattices. e,f) 2D GISAXS scattering pattern and SEM of (110)-oriented bcc superlattices. Scale bars for the SEM top-down and cross-section views are 200 nm and 100 nm, respectively (d,g).

We first analyzed surface-confined growth of superlattices on DNA-modified substrates that presented a B-type linker. For this mono-functionalized substrate, superlattices grown through five half-cycles resulted in a (100)-oriented polycrystalline bcc film (Figures 26b-e). This observation can be understood in terms of maximizing DNA duplexes at the substrate-superlattice interface. In principle, planes with higher packing densities result in increased bonding between the superlattice and substrate. For a bcc crystal, the (110) plane has the highest packing density, followed closely by the (100) plane. Note, however, that the crystal symmetry of these superlattices is defined by the position and type of inorganic core; thus, while the AuNPs form a bcc lattice, the binary linker design results in an SNA lattice isostructural with CsCl. The interfacial energy is then inversely proportional not to the planar packing density of all particles in the system, but solely to the density of particles that can

bind to the substrate. For B-type substrates, the planar packing density of complementary A-type particles with bcc (100) texture is $1/a^2$ (where a is the lattice parameter) and is therefore favored over the (110) texture, which has a density of $1/(\sqrt{2})a^2$ (compare Figures 26c and 26g). Another way to state this is that the (100) plane, although less densely packed, is comprised entirely of particles that can hybridize to the B-type substrate. While particles in the (110) plane are more densely packed, only half can engage in attractive hybridization interactions.

In contrast to the previous system, the surface can also be functionalized with both A- and B-type linkers. For these bi-functionalized substrates that can bind both particle types, the (110) plane has the highest packing density ($2/(\sqrt{2})a^2$) of substrate-binding particles (Figure 26g). Therefore these surfaces should direct the growth of crystals with (110) texture, which matches experimental observations (Figures 26f-i).

An interesting aspect of this novel system is that one can track the crystal phases present as a function of the substrate linker ratio (Figure 27). Here, the substrate linker ratio is defined as the ratio of B to A-type linkers on the substrate. At low growth temperatures, kinetically trapped structures are formed that consist of mostly amorphous aggregates (green region in Figure 27a), while crystal growth near the melting temperature (T_m , the temperature at which the superlattice dissociates) results in monolayer formation (gray region in Figure 27a). Superlattice growth at several degrees below T_m resulted in (100)- or (110)-oriented crystals depending on the substrate linker ratio (red and blue regions in Figure 27a). The relative stabilities of each orientation can be determined by comparing the number of superlattice-substrate duplexed interconnects for each orientation using the Complementary Contact Model (CCM), modified to include interfacial interactions (Figure 10b). This simple geometrical model based on complementary hybridization interactions can be used to predict various crystal phases under ideal annealing conditions. Significantly, the model predicts a crossing point in the relative stability of (100)- and (110)-orientated superlattices at a substrate linker ratio of 85B:15A, which was confirmed experimentally. This result demonstrates that these structures are likely the thermodynamic products. Interestingly, (110)-textured phases are observed at low temperatures on mono-functionalized substrates, which can be attributed to strain and low particle mobility at these growth temperatures.

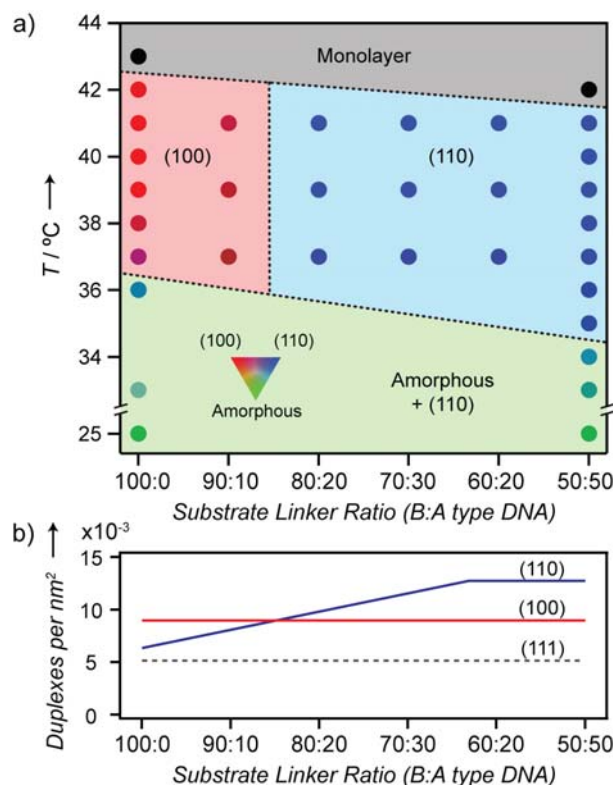


Figure 27. a) Crystallographic phase behavior for bcc thin-film superlattices depends on both growth temperature and the substrate linker ratio. All data are for 5 half-cycles of crystal growth. The relative concentration of (100), (110) and amorphous phases were determined by fitting experimental GISAXS data and set to a RGB color scale. Under annealing conditions (red, blue regions), the orientation depends on the type of interfacial DNA-bonding interactions, while at low temperatures amorphous structures are formed. The dashed lines and coloring are a guide for the eye. b) The relative stability of each orientation can be determined using the CCM model, confirmed experimentally in (a). For reference, the (111) orientation with the next highest planar packing density is included.

To better understand the growth process of the nanoparticle thin-film superlattices, GISAXS was used to monitor each step of the assembly process (Figure 28). Several distinct nanoparticle arrangements were observed on B-type substrates during growth at optimal temperatures (40 °C), and all were found to maximize the number of particle-substrate and particle-particle DNA interconnects. For a two-dimensional assembly of repulsive spheres (a single layer of particles), a hexagonal arrangement maximizes particle density. Indeed, after one half-cycle the in-plane scattering peaks at $q = 0.020$ and 0.040 \AA^{-1} can be attributed to a disordered hexagonal structure with an average interparticle distance of 36 nm (Figures 28a,b).

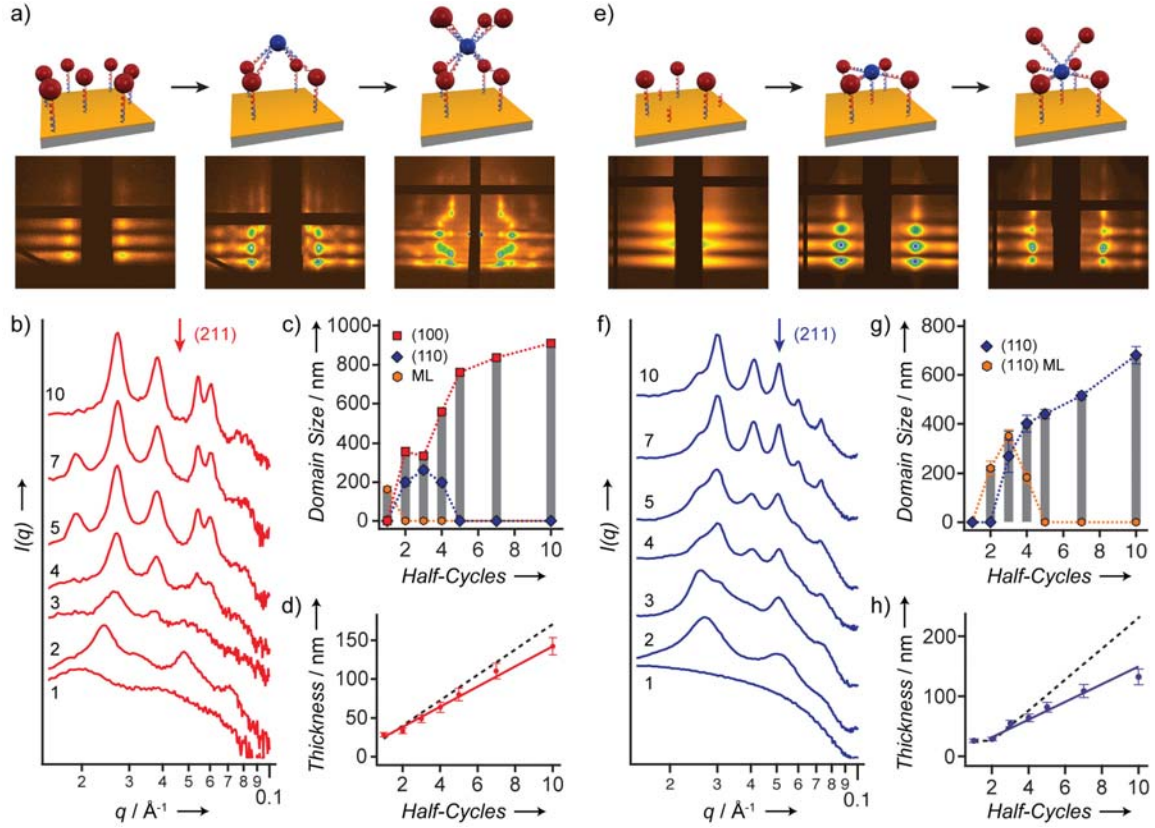


Figure 28. Stepwise GISAXS characterization of (100)- and (110)-textured bcc superlattices. a,e) Idealized schematic and 2D GISAXS scattering patterns after 1, 2 and 3 half deposition-cycles on mono-functionalized (100)-directing and bi-functionalized (110)-directing DNA substrates, respectively. b,f) Normalized GISAXS horizontal linecuts at $\alpha_f = \alpha_i$ after successive half-cycles on mono-functionalized and bi-functionalized DNA substrates, respectively. The curves are offset for clarity and plotted on a log-log scale. Note the systematic absence (b) or presence (f) of the (211) peak that can be used as a diagnostic for determining crystallographic orientation. The peaks at $q = 0.02$ (b, 5 and 7 half-cycles) and $q = 0.023$ (f, 7 and 10 half-cycles) are from diffuse scattering and are not attributed to the particle arrangement. The crystal grain sizes increase with deposition cycles, both in the plane of the substrate (c,g) and out of the plane (d,h), for (100) and (110)-textured superlattices, respectively. The gray bars in (c,g) show average domain size, while the colored markers show various structures deconvoluted from the GISAXS line cuts (“ML” denotes the presence of a monolayer). Error bars are determined from the standard deviation of at least three separate measurements, and in many cases are smaller than the marker size. The dashed lines in (d,h) show the expected film thickness if a full layer were deposited per half-cycle.

After the second half-deposition cycle on a B-type substrate, three-dimensional ordering consisting of two interpenetrating square lattices was observed (Figures 28a,b), which is equivalent to a bcc (100) crystal with two particles layers. This structure results from particles in the first layer simultaneously maximizing the number of nearest neighbors (4) and the areal density of particle-substrate interactions. SEM imaging of these two-layer samples show 2-dimensional aggregation with fractal morphology. During the transition from a disordered hexagonal monolayer to a square array, the particles in the first layer must densify. If this reorganization process is hindered by low particle mobility, the structure will become

strained, which results in a larger in-plane lattice parameter for these two-layer structures (35.0 ± 0.5 nm) than would be expected from both multilayered films (32.7 ± 0.1 nm) and bulk 3D superlattices with the same nanoparticle size and DNA sequence (29.5 ± 0.2 nm). An increase in this tensile strain (e.g. at lower growth temperatures) promotes the growth of the lower density (110) orientation (Figure 10, 100B:0A, 36 °C).

Remarkably, after only three half-cycles, the GISAXS scattering pattern is dominated by (100)-oriented crystals consisting of a single unit cell in the out-of-plane direction. Simultaneously, the in-plane lattice parameter contracts as additional duplexed DNA linkages stabilize the crystal. Though some instability in the first few layers results in the presence of (110)-textured particle arrangements, subsequent growth resulted in exclusively (100) oriented superlattice films (Figure 28c). We observed a linear increase in film thickness with deposition cycles, in addition to a narrowing of the scattering peaks. The assemblies therefore form more ordered structures and grow in size as additional particle layers are added, as expected from standard thin-film crystal growth models (Figures 28b,c).

The same step-by-step analysis for bi-functionalized substrates with a 50B:50A substrate linker ratio was used to elucidate the difference in growth mechanisms on substrates that could bind both particles (Figures 28d-f). We observed a sub-monolayer of particles after a single half-deposition-cycle with interparticle distances that were too large to be observed by GISAXS (> 150 nm). This low particle density is attributed to the 2-fold decrease in substrate-bound DNA linkers, which makes particle-substrate interactions less favorable. The decrease in attractive interaction is also observed by monitoring the thermal desorption transition, which broadens and shifts to lower temperatures compared to the desorption of SNA-AuNPs from mono-functionalized DNA substrates. In the context of superlattice growth, this sub-monolayer acts as a seed layer, such that after two half-cycles, only two-dimensional aggregation occurs with no increase in film thickness. The structure is consistent with the (110) plane of a bcc crystal, and the characteristic first order scattering peak at $q = 0.024 \text{ \AA}^{-1}$ was observed through the first four half-cycles (Figure 11e). The presence of this monolayer after several deposition cycles indicates island formation, which is often observed when substrate-particle interactions are weaker than particle-particle interactions. Three-dimensional ordering with bcc symmetry (q_0 at 0.028 \AA^{-1}) was first observed with as little as two crystal layers, which here occurred after three half-cycles. As before, subsequent growth resulted in a linear increase in film thickness with deposition cycles and crystallite in- plane growth (Figures 28g,h).

We have demonstrated that DNA-mediated crystallization can be used to provide a simplified model for understanding crystal growth in which adlayers display direct bonding interactions with a substrate but lack the periodic potential inherent to atomic systems. The interfacial energy between a thin-film superlattice and the substrate, and consequently the orientation, can be controlled by appropriate choice of DNA interconnects. This work creates a new design rule for these structures: the orientations of such programmable crystalline thin-films will be dictated by the crystal planes that maximize complementary interactions with the substrate. This strategy could easily be applied to other binary crystal symmetries, or to surfaces patterned with DNA for lithographically templating nanoparticle superlattices. Furthermore, the ideas set forth in this work suggest a route for growing single crystal nanoparticle superlattices by controlling epitaxial processes. We have also shown that the number of layers in SNA-NP superlattice thin films can be controlled, which is useful for determining thickness-dependent materials properties. The additional level of control extended to the system through direct substrate-adlayer bonding interactions will be

important for the development of materials that take advantage of the periodicity of the inorganic core material, such as optical metamaterials, photonic bandgap materials, and magnetic storage media.

2.9 Capillary-driven nanowire immobilization - Hong

There has been an increasing interest in the synthesis and applications of anisotropic nanoparticles, due to their rich plasmonic, optoelectronic, and catalytic properties. Among them, OWL-generated gapped nanowires developed by Mirkin *et al.* show great promise in several areas, including surface enhanced Raman spectroscopy (SERS) and molecular electronics. The Mirkin group has shown the capability of tuning plasmonics of these nanostructures by adjusting the gap size and length of respective metal segments. It's also been recently shown that these gapped nanowires can be used as nanomasks for fabricating nanogaps in graphene nanostructures, potentially useful for graphene electronics. However, in order to realize the full potential of these OWL nanostructures, it is imperative to align them on a large area with control over orientation and position. For example, ordered nanostructures on a desired substrate can be used to create optical and electronic devices. Although there have been several efforts to align OWL nanostructures, large-area alignment has been lacking. By using nanoscale capillary force that has been shown to align chemically synthesized gold nanorods, this work demonstrates that OWL nanostructures with varied dimensions, including gap size and wire length, can be aligned to lithographically-generated PDMS templates. These aligned OWL nanostructures can then be transferred to target substrates, as SERS substrates for small organic molecules or as nanomasks for fabrication of arrays of gapped graphene nanoribbons. Further studies of polarization-dependent SERS and fabrication of SERS nanosheets with controlled nanostructure density and orientation will ensue.

As has been reported in the assembly of gold nanorods and also found in our study, it is essential to functionalize the electrochemically-synthesized multi-segmented metal nanowires with surfactants. CTAB was used in this study as a surfactant for several reasons: First, without CTAB functionalization, the nanowires cannot be easily dispersed and aggregate due to strong van der Waals interactions. Second, we found that CTAB is critical during the alignment process, without which the nanowires cannot be well aligned. Although CTAB has been extensively used in the synthesis of gold nanostructures, such as nanorods and prisms, it has not been reported how CTAB can be functionalized to electrochemically-synthesized gold nanowires. We have functionalized these nanowires by incubation of the nanowires in 0.45 mM CTAB aqueous solution after dissolution from AAO template. We found that repeated exchange (up to 8 iterations) of new CTAB solution is required for successful coating, which can be judged by the fact that the nanowires remain pseudo-liquid when centrifuged and can be easily dispersed when adding new CTAB solution (without need of sonication).

Scanning electron microscopy (SEM) images (Figure 29) show the alignment of nanowire 1 (Figures 29A and B) and nanowire 2 ((Figures 29C and D) on PDMS stamps can be accomplished with high yield and good control over orientation and position. It is interesting to mention that although the size of linelet features in PDMS is much larger than that of the nanowires, the nanowires are well aligned both vertically and horizontally, (compare row 1 and 2 in Figure 29B). This is achieved since all nanowires are aligned to the same side of the linelet trenches, which can be explained by the fact the nanowires are

dragged to the same direction when the nanowire droplet moves over the trenches. This result manifests the advantage of this technique since there is no need to exactly match the linelet size to that of the nanowires. However, it was also found that multiple nanowires can be aligned to a single trench if the trench is too wide (Figure 29E).

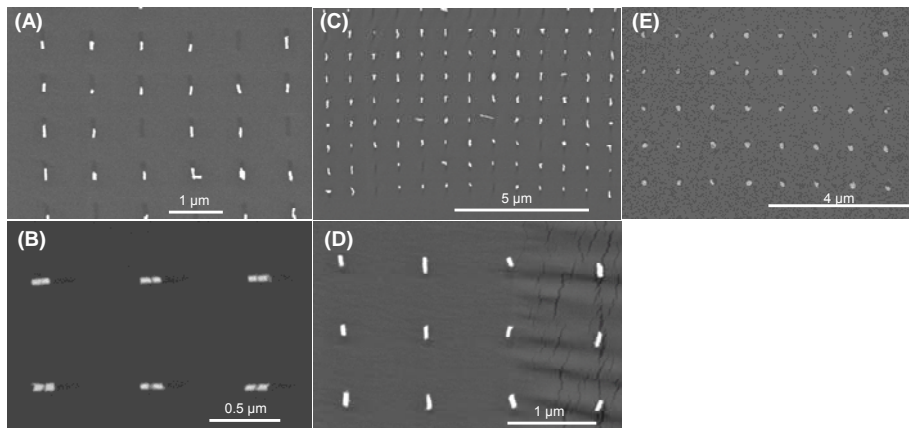


Figure 29. (A, B) Nanowire 1 (80 nm Au/20 nm Ni/80 nm Au) are aligned to linelets with a length of 500 nm. (C, D) Nanowire 2 (60 nm Au/1-2 nm Ni/60 nm Au) are aligned to linelets with a length of 350 nm. (E) Multiple nanowires are aligned to a single linelet trench when the width of the trench >150 nm.

We also observed that the OWL nanowires can be well aligned even they don't form crystalline structures at the drop edge, which has been reported to be essential for the alignment of chemically synthesized gold nanorods. SEM images of the dried drop edge for both OWL nanowires and gold nanorods (purchased from Nanopartz) clearly show the difference wherein Nanopartz gold nanorods form highly crystalline structures (Figure 30A) while OWL nanowires does not (Figure 30B).

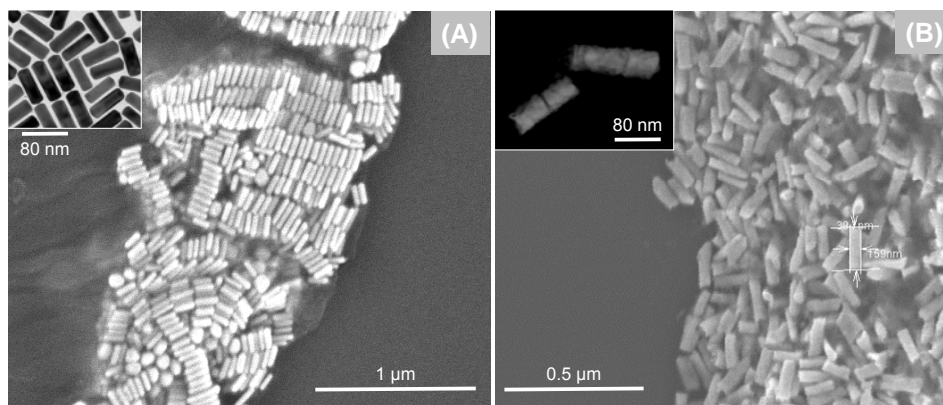


Figure 30. (A) Nanopartz gold nanorods form crystalline structure at the dried drop edge. (B) Nanowire 1 (60 nm Au/1-2 nm Ni/60 nm Au) don't form crystalline structure at the dried drop edge.

Upon the successful alignment of the nanowires, we then transferred the nanowires to surfaces containing small organic molecules for SERS detection by microcontact printing,

Figure 31B (iv) and Figure 31A. A PMMA layer was used as an adhesion layer to receive the nanowires. The nanowire 2 was chosen because of its plasmonic resonance at 785 nm, the wavelength of the laser used in SERS study. The Ni segment in the nanowire was etched in HCl after transfer. Raman mapping on the regions of the transferred nanowires clearly show enhanced Raman signal for the small molecule (non-enhanced regions not shown here). This result opens the possibility of fabricating SERS nanosheets with aligned nanowires.

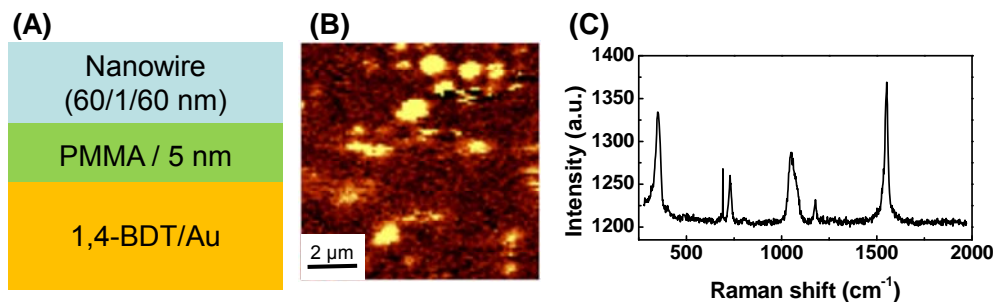


Figure 31. (A) Nanowires are transferred to 1,4-BDT surface. Thin layer of PMMA will not affect the plasmonic enhancement effect of the gapped nanowires to 1,4-BDT. (B, C) Raman mapping and spectrum of 1,4-BDT. The Raman mapping is integrated to the band around $\sim 1560 \text{ cm}^{-1}$.

In addition, we have successfully transferred the aligned nanowires to graphene substrates for the fabrication of gapped nanoribbons. We have initially shown that arrays of graphene nanoribbons without gaps can be obtained when gold nanorods without gaps are used as nanomasks in the etching process. The next step will be fabrication of gapped graphene nanoribbons and utilization of them in graphene electronics (Figure 32).

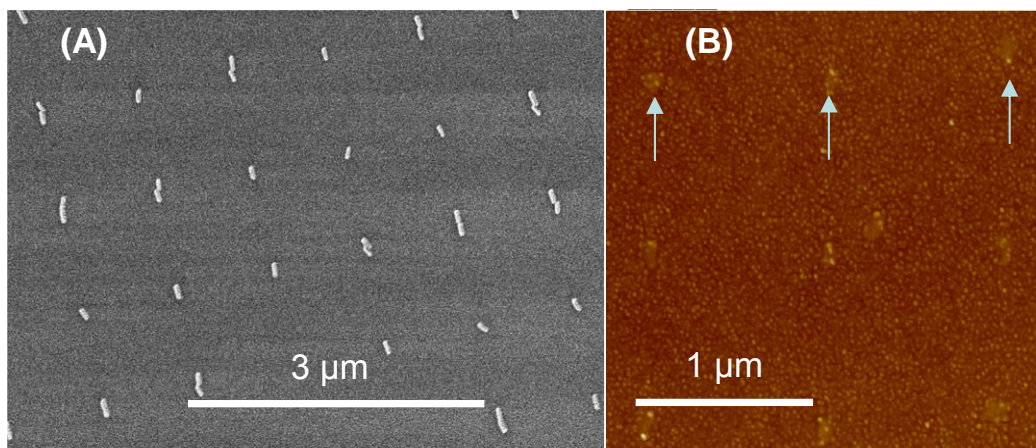


Figure 32. (A) Nanowires transferred to graphene substrate. (B) 3×3 array of graphene nanoribbons. The 3 arrows indicate the upper row with 3 ribbons.

In a related set of experiments, CNT-bridged nanowires were immobilized in trenches that were lithographically defined in polymethyl methacrylate (PMMA) (Figure 33). As a proof-of-concept, trenches were defined by e-beam lithography on a silicon oxide substrate. A suspension of nanowires in isopropyl alcohol was drop-cast

on the trench array. After the solvent was evaporated, the nanowires were manually brushed across the trench arrays several times with constant applied pressure, which led to their eventual alignment within the trenches. Nanowires remaining outside the trenches are subsequently removed with the e-beam resist in the lift-off process. After removing the e-beam resist, Ni segment of the carbon nanotube functionalized nanowire was etched.

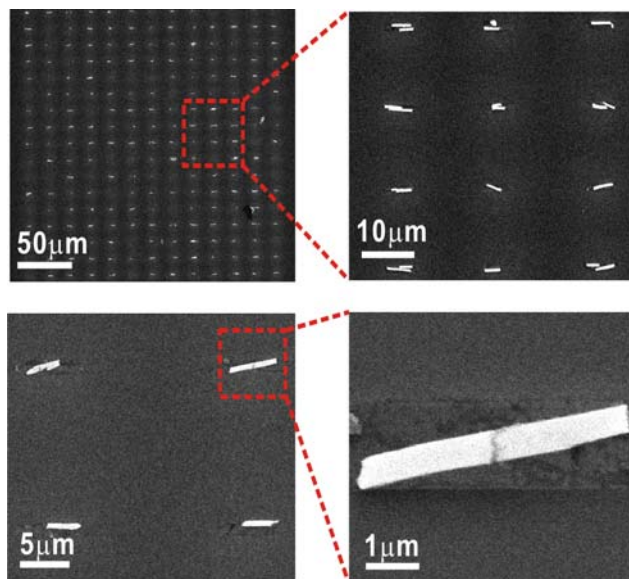


Figure 33. SEM images of multi-segmented nanowire functionalized with carbon nanotubes.

SEM images confirmed the alignment of individual wires or collections of nanowires (Figure 33 in registry with the e-beam defined lithographic patterns. Here, the degree of integration was 100 1/cm^2 and about 80% of carbon nanotube remained undamaged. Therefore, we have demonstrated a facile method to massively align nanowires functionalized with carbon nanotubes.

Summary

In conclusion, we report a facile strategy to fabricate and self-assemble multi-segmented nanowires functionalized with various substances, such as carbon nanotubes, polypyrroles and motor proteins. The methods developed in the scope of this grant allow one to mass produce NBWs, including single or multiple CNT channels with controlled length. Through the mechanical alignment strategy, carbon nanotube bridged wires could be localized and aligned into specific position on the substrate. Functionalizing the NBWs with biological receptors provides a simple fabrication route to biosensors that could detect DNA, biotin and hexanal that may bear clinical importance. Additionally, the broad classes of devices that are now possible through the combination of DNA- or capillary-mediated rational assembly and functional gapped nanowires stand poised to make a large impact on real-time chemical sensing. The collaborative approach between the Mirkin and Hong groups was crucial to the success of this grant.

These strategies should provide great opportunities in various areas, such as drug delivery systems, biosensors and biochips for the controlled release of chemicals to bio-systems. This work will lead to significant fundamental advances that will drive the development of new and useful technology. Anticipated payoffs include: materials for encoding and encrypting high value structures, nanoelectronic devices, new ways of propagating light through nanostructures, compact power generation sources, high sensitivity and selectivity diagnostic tools for pathogenic and toxic agents including those involved in bio-warfare and bioterrorism, and templates that can be used to control the assembly and positioning of nanostructures into a wide range of functional materials and devices. Massively parallel nanotemplates have the potential to revolutionize many aspects of molecular biology, surface science, and materials science. They will allow one to manipulate architectures, synthetic and living, often at the single particle elementary building block level.

List of Publications and Significant Collaborations that resulted from your AOARD supported project: In standard format showing authors, title, journal, issue, pages, and date, for each category list the following:

a) Papers published in peer-reviewed journals

Mirkin and Hong

1. Liao, X.; Brown, K. A.; Schmucker, A. L.; Liu, G.; He, S.; Shim, W.; Mirkin, C. A. "The Desktop Fab," *Nature*, **2013**, in press.
2. Senesi, A. J.; Eichelsdoerfer, D. J.; Macfarlane, R. J.; Jones, M. R.; Auyeung, E.; Lee, B.; Mirkin, C. A. "Stepwise evolution of programmable DNA-nanoparticle superlattices," *Nature Nanotechnol.*, **2013**, in press.
3. Kim, E.; Byun, K. E.; Choi, D. S.; Lee, D. J.; Cho, D. H.; Lee, B. Y.; Yang, H.; Heo, J.; Chung, H.-J.; Seo, S.; Hong, S. "Electrical control of kinesin-microtubule motility using a transparent functionalized-graphene substrate," *Nanotechnology*, **2013**, *24*, 195102.
4. Zhou, X.; He, S.; Brown, K. A.; Arroyo, J.; Boey, F.; Mirkin, C. A. "Locally Altering the Electronic Properties of Graphene By Nanoscopically Doping It With Rhodamine 6G," *Nano Lett.*, **2013**, *13*, 1616–1621.
5. Liu, G.; Zhou, Y.; Banga, R. S.; Boya, R.; Brown, K. A.; Chipre, A. J.; Nguyen, S. T.; Mirkin, C. A. "The role of viscosity on polymer ink transport in dip-pen nanolithography," *Chem. Sci.*, **2013**, *4*, 2093-2099.
6. Schmucker, A. L.; Barin, G.; Brown, K. A.; Rycenga, M. J.; Coskun, A.; Buyukcakir, O.; Osberg, K. D.; Stoddart, J. F.; Mirkin, C. A. "Electronic and Optical Vibrational Spectroscopy of Molecular Tunnel Junctions Created by On-Wire Lithography," *Small*, **2013**, DOI: 10.1002/sml.201201993.
7. Shim, W.; Brown, K. A.; Zhou, X.; Rasin, B.; Liao, X.; Schmucker, A. L.; Mirkin, C. A. "Plow and Ridge Nanofabrication," *Small*, **2013**, DOI: 10.1002/sml.201203014.
8. Shim, W.; Brown, K. A.; Rasin, B.; Liao, X.; Zhou, X.; Mirkin, C. A. "Multifunctional cantilever-free scanning probe arrays coated with multilayer graphene," *Proc. Natl. Aca. Sci. USA*, **2012**, *109*, 18312-18317.
9. Park, S. Y.; Kang, B.-S.; Hong, S. "Improved neural differentiation of human mesenchymal stem cells interfaced with carbon nanotube scaffolds," *Nanomedicine*, **2013**, *8*, 715-723.
10. Heo, K.; Lee, H.; Park, Y.; Park, J.; Lim, H.-J.; Yoon, D.; Lee, C.; Kim, M.; Cheong,

- H.; Park, J.; Jian, J.; Hong, S. "Aligned networks of cadmium sulfide nanowires for highly flexible photodetectors with improved photoconductive responses," *J. Mater. Chem.*, **2012**, *22*, 2173-2179.
11. Park, J.; Lim, J. H.; Jin, H. J.; Namgung, S.; Lee, S. H.; Park, T. H.; Hong, S. "Bioelectronic sensor based on canine olfactory nanovesicle -carbon nanotube hybrid structures for the fast assessment of food quality," *Analyst*, **2012**, 3249-3254.
 12. Jin, H. J.; Lee, S. H.; Kim, T. H.; Park, J.; Song, H. S.; Park, T. H.; Hong, S. "Nanovesicle-based bioelectronic nose platform mimicking human olfactory signal transduction," *Biosensors and Bioelectronics*, **2012**, *35*, 335-341.
 13. Zhou, X.; Shade, C. M.; Schmucker, A. L.; Brown, K. A.; He, S.; Boey, F. Y. C.; Ma, J.; Zhang, H.; Mirkin, C. A. "OWL-Based Nanomasks for Preparing Graphene Ribbons with Sub-10 nm Gaps," *Nano Lett.*, **2012**, *12*, 4734-4737.
 14. Lee, B. Y.; Heo, K.; Schmucker, A. L.; Jin, H. J.; Lim, J. K.; Kim, T.; Lee, H.; Jeon, K.-S.; Suh, Y.; Mirkin, C. A.; Hong, S. "Nanotube Bridged Wires," *Nano Lett.*, **2012**, *12*, 1879-1884.
 15. Wong, L.-S.; Karthikeyan, C. V.; Eichelsdoerfer, D. J.; Micklefield, J.; Mirkin, C. A. "A Methodology for Preparing Nanostructured Biomolecular Interfaces with High Enzymatic Activity," *Nanoscale*, **2012**, *4*, 659-666.
 16. Choi, D. S.; Byun, K.-E.; Hong, S. "Dual Transport Systems based on Hybrid Nanostructures of Microtubules and Actin Filaments," *Small*, **2011**, *7*, 1755-1760.
 17. Baik, K. Y.; Park, S. Y.; Heo, K.; Lee, K.-B.; Hong, S. "Carbon Nanotube Monolayer Cues for Osteogenesis of Mesenchymal Stem Cells," *Small*, **2011**, *7*, 741-745.
 18. Arif, M.; Heo, K.; Lee, B. Y.; Lee, J.; Seo, D. H.; Seo, S.; Jian, J.; Hong, S. "Metallic nanowire-graphene hybrid nanostructures for highly-flexible field emission devices", *Nanotechnology*, **2011**, *22*, 355709.
 19. Sung, M. G.; Lee, H.; Heo, K.; Byun, K.-E.; Kim, T.; Seo, D. H.; Seo, S.; Hong, S. "Scanning Noise Microscopy on Graphene Devices," *ACS Nano*, **2011**, *5*, 8620-8628.
 20. Byun, K.-E.; Choi, D. S.; Kim, E.; Seo, D. H.; Yang, H.; Seo, S.; Hong, S. "Graphene-Polymer Hybrid Nanostructure-Based Bioenergy Storage Device for Real-Time Control of Biological Motor Activity," *ACS Nano*, **2011**, *5*, 8656-8664.
 21. Lim, J. K.; Lee, B. Y.; Pedano, M. L.; Senesi, A. J.; Jang, J.-W.; Shim, W.; Hong, S.; Mirkin, C. A. "Alignment Strategies for the Assembly of Nanowires with Submicron Diameters," *Small*, **2010**, *6*, 1736-1740.

b) papers published in peer-reviewed conference proceedings,

None.

c) papers published in non-peer-reviewed journals and conference proceedings,

None

d) conference presentations without papers,

Mirkin

1. Ohio State University, Columbus, OH; "Programming Materials Synthesis with DNA: Applications in Biology and Medicine," and "Unconventional Approaches to Nanofabrication," (2010).

2. Pittcon Conference, Orlando, FL; "Multiplexed Detection with Nanodisk Codes," and "Nanoflares: A New Modality in Biodiagnostics and Bioimaging," (2010).
3. 237th ACS National Meeting, San Francisco, CA; "Nanoflares for the Intracellular Detection of Small Molecules, Nucleic Acids, Metal Ions, and Protein Targets," and "Anisotropic Nobel Metal Nanostructures," (2010).
4. University of California – Berkeley, Berkeley, CA; "Programming the Assembly of Nanoparticles with DNA: The Atom Analogy," (2010).
5. Herman S. Bloch Memorial Lecture, University of Chicago, Chicago, IL; "Molecular Printing: A Chemist's Approach to Desk Top Fab," (2010).
6. 101st American Association for Cancer Research (AACR) Annual Meeting, Washington, DC; "The Polyvalent Nanoparticle Conjugate: A New Frontier in Cancer Diagnostics and Therapeutics," (2010).
7. James Madison University, Harrisonburg, VA; "Nanotechnology: Small Wonders, Medical Miracles," (2010).
8. University of Kentucky, Lexington, KY; "Programming Materials Synthesis with DNA: Applications in Biology and Medicine," (2010).
9. Feinberg School of Medicine's Distinguished Lecture in Life Sciences, Northwestern University, Chicago, IL; "The Polyvalent Gold Nanoparticle Conjugate: A New Paradigm in Molecular Diagnostics and Intracellular Gene Regulation," (2010).
10. Keck Seminar, Gordon Research Conference, Houston, TX; "Polyvalent DNA Nanostructures: A New Frontier in Materials Synthesis, Biodiagnostics, and Intracellular Gene Regulation," (2010).
11. Digestive Disease Week for Society for Surgery of the Alimentary Tract, New Orleans, LA; "Nanotechnology in Biology and Medicine," (2010).
12. 54th International Conference on Electron, Ion, & Proton Beam Technology & Nanofabrication, Anchorage, Alaska; "Molecular Printing: A Chemist's Approach to a Desk Top Fab," (2010).
13. Gordon Research Conference on Noble Metal Nanoparticles, Mount Holyoke College, South Hadley, MA; Alexander M. Cruickshank Lecture on "Nanoparticle Bioconjugates: A New Frontier in Materials Science, Biology, and Medicine," (2010).
14. Gordon Research Conference on Plasmonics, Colby College, Waterville, Maine; "Chemical Approaches to Making Plasmonically Active Nanostructures," (2010).
15. ACS National Meeting, Boston, MA, "Towards a Desktop Fab: Polymer Pen Lithography and Beam Pen Lithography," "DNA-Programmable Assembly of Colloidal Crystals," "Nanoflares: A New Modality in Biodiagnostics and Bioimaging," and "Oligonucleotide-Gold Nanoparticles Conjugates as Intracellular Gene Regulation Agents," (2010).
16. IEEE Nano 2010/Nano Korea 2010, Seoul, Korea, "Molecular Printing: A Chemist's Approach to Desktop Fab," (2010).
17. University of Calgary, Calgary, Alberta, Canada, "The Polyvalent Gold Nanoparticle Conjugate: Materials Synthesis, Biodiagnostics, and Intracellular Gene Regulation," and "Molecular Printing: A Chemist's Approach to a Desk Top Fab," (2010).
18. Scripps Research Institute, La Jolla, CA, "Polyvalent DNA: A New Frontier in Molecular Diagnostics and Intracellular Gene Regulation," (2010).
19. The Pennsylvania State University, State College, PA, "Polyvalent DNA Nanostructures: A New Frontier in Materials Synthesis, Biodiagnostics, and Intracellular Gene Regulation," (2010).

20. Materials Research Society Fall Meeting, Boston, MA, "Oligonucleotide-Gold Nanoparticle Conjugates as Probes for Intracellular Diagnostics and Gene Regulation," (2010).
21. Einstein Award Lecture, Chinese Academy of Sciences, Beijing, China, "The Polyvalent Oligonucleotide Nanoparticle Conjugate: A New Frontier in Materials Synthesis, In Vitro Diagnostics, and Intracellular Gene Regulation," (2010).
22. Xiamen University, Xiamen, China, "Plasmonic Seeds: a Novel Strategy for Synthesizing Anisotropic Nobel Metal Nanostructures," (2010).
23. Pacifichem, Honolulu, HI, "Nanostructure Synthesis with Plasmonic Seeds", "Coordination-Based Abiotic Molecular Machines", and "Novel Forms of Biolabeling and Amplification Afforded by Structures Generated by On-Wire Lithography," (2010).
24. Gordon Research Conference, Ventura, CA, "Scanning Probe Block Copolymer Lithography," (2011).
25. AACR, Miami, FL, "Polyvalent DNA Nanostructures: New Modalities in Cancer Diagnostics and Therapeutics," (2011).
26. University of New Mexico, Chemistry Department Colloquium, Albuquerque, NM, "The Polyvalent Gold Nanoparticle Conjugate: Materials Synthesis, Biodiagnostics, and Intracellular Gene Regulation," (2011).
27. Sandia National Labs, Truman Lecture, Albuquerque, NM, "Molecular Printing: A Chemist's Approach a Desk Top Fab," (2011).
28. Lab Automation Conference, Palm Springs, CA, "The Polyvalent Oligonucleotide Nanoparticle Conjugate: A New Frontier in In Vitro Diagnostics and Intracellular Gene Regulation," (2011).
29. Pittcon Conference, Atlanta, GA, "Polyvalent DNA Architecture: New Modalities for Intracellular Gene Regulation and Detection" (Plenary Lecture), and "Intracellular Detection by Nano-Flares," (2011).
30. American Academy of Allergy, Asthma & Immunology Annual Meeting, San Francisco, CA, "Polyvalent DNA: A New Paradigm in Molecular Diagnostics and Intracellular Gene Regulation," (2011).
31. American Association for Cancer Research Annual Meeting, Orlando, FL, "Ultrasensitive Approaches to the Early Detection of Cancer," (2011).
32. National Institute of Standards and Technology, Gaithersburg, MD, "The Polyvalent Gold Nanoparticle Conjugate: Material Synthesis, Biodiagnostics, and Intracellular Gene Regulation," (2011).
33. Walter J. Chute Lecture, Dalhousie University, Halifax, Nova Scotia, Canada; "A Chemist's Approach to Nanofabrication: Towards a Desktop Fab" and "Spherical Nucleic Acid (SNA) Nanostructures: Establishing New Paradigms in Molecular Diagnostics and Intracellular Gene Regulation" (2011).
34. Van't Hoff Lecture, CHAINS 2011, DeFabrique, Maarssen, Holland "Spherical Nucleic Acid (SNA) Nanostructures: Establishing a New Paradigm in Materials Synthesis, Molecular Diagnostics, and Intracellular Gene Regulation" (2011).
35. University of Illinois at Champaign-Urbana, Chemistry Department Seminar, Urbana, IL, "Polyvalent Nucleic Acids Nanostructures for Detection and Intracellular Gene Regulation" (2011).
36. NUtch Ventures, Annual Innovator's Dinner, Lincoln, NE, "Innovation in Nanotechnology: Separating Hype from Real Opportunity," (2011).

37. 10th US-Korea Workshop on Nanostructured Materials, 8th US-Korea Workshop on Nanoelectronics, and NBIT Program Review, Gyeongju, Korea, "Massively Parallel Nanostructure Assembly," (2011).
38. Technologies for Future Micro Nano Manufacturing, Napa Valley, CA, "The Evolution of Scanning Probe Molecular Printing" (2011).
39. ACS National Meeting, Denver, CO, "Plasmon-Mediated Syntheses of Silver Nanostructures" (2011).
40. Bio-X STT-TAGGANTS Review, Dayton, OH, "Biobarcode and Nanoflares: New Nanotechnological Taggant Approaches" (2011).
41. Wright State University, Dayton, OH, "Polyvalent Nucleic Acids Nanostructures for Detection and Intracellular Gene Regulation" (2011).
42. University of Texas, Austin, TX, "Spherical Nucleic Acid Nanostructures: Establishing a New Paradigm in Materials Synthesis, Molecular Synthesis, Molecular Diagnostics, and Intracellular Gene Regulation" (2011).
43. University of Maryland, Baltimore, Translational Genomes to Personalized Medicine Symposium, Baltimore, MD, "Spherical and other Three-dimensional Forms of Nucleic Acids: A New Gene Regulation Platform" (2011).
44. Loyola University Chicago Science Week, Chicago, IL, "A Chemist's Approach to Nanofabrication: Towards a "Desktop Fab" (2011).
45. MSKCC'S Nanotechnology Center Retreat, New York, NY, "Spherical Nucleic Acid (SNA) Nanostructures: Establishing New Paradigms in Molecular Diagnostics and Intracellular Gene Regulation" (2011).
46. 11th US-Japan Symposium on Drug Delivery Systems, Maui, Hawaii, "Spherical Nucleic Acid (SNA) Nanostructures: Establishing New Paradigms in Molecular Diagnostics and Intracellular Gene Regulation" (2011).
47. NDIA for the 25th Anniversary of the MURI Program, Washington, DC; "MURI-Funded Scientific and Technological Blockbusters from Northwestern University" (2011).
48. Eindhoven University of Technology, Eindhoven, The Netherlands; "A Chemist's Approach to Nanofabrication: Towards a "Desktop Fab" (2011).
49. AFOSR Program Review, National Harbor-Oxon Hill, MD; "Dip-Pen Nanolithography Generated Combinatorial Libraries" (2011).
50. AFOSR Program Review, National Harbor-Oxon Hill, MD; "MURI: BioProgrammable One-, Two-, and Three-Dimensional Materials" (2011).
51. TBN Program Review, San Diego, CA; "Scanning Probe Epitaxy" (2012).
52. APS National Meeting, Boston, MA; "Nanoparticle Superlattice Engineering with DNA" (2012).
53. APS National Meeting, Boston, MA; "Having Your Cake and Eating it Too; Effective Engagement in Start-Ups from an Academic Seat" (2012).
54. AFOSR Spring Review, Arlington, VA; "Nanotechnology: Moving Beyond Small Thinking" (2012).
55. PITTCON, Orlando, FL; "Single-Cell Analysis of Intracellular Content with "Nano-Flares" (2012).
56. ICOMM NU Conference, Northwestern University, Evanston, IL; "A Chemist's Approach to Nanofabrication: Towards a "Desktop Fab" (2012).
57. NEO Winter Meeting, Skokie, IL; "Innovation in Nanotechnology: Separating Hype from Real Opportunity," (2012).

58. AFOSR Spring Program Review, Arlington, VA; "A Chemist's Approach to Nanofabrication: Towards a "Desktop Fab" (2012).
59. Erik B. Young Lecture, University of Maryland, College Park, College Park, MD; "Spherical Nucleic Acid (SNA) Nanostructures: Establishing New Paradigms in Materials Synthesis, Molecular Diagnostics, and Intracellular Gene Regulation" (2012).
60. ACS 243rd National Meeting, San Diego, CA; "Advances in Dip-Pen Nanolithography: Toward High-Throughput, Low Cost, Centimeter Scale Desktop Nanofabrication and Molecular Printing" (2012).
61. ACS 243rd National Meeting, San Diego, CA; "Single-Cell Analysis of Intracellular Content with "Nano-Flares" (2012).
62. ACS 243rd National Meeting, San Diego, CA, ACS Award for Creative Invention; "Spherical Nucleic Acid (SNA) Nanostructures: Establishing a New Paradigm in Materials Synthesis, Molecular Diagnostics, and Intracellular Gene Regulation" (2012).
63. ACS 243rd National Meeting, San Diego, CA; "Allosterically Regulated Supramolecular Assemblies Synthesized via the Weak-link Approach (WLA)" (2012).
64. MRS Spring Meeting, San Francisco, CA; "Nano-flares for the Analysis of Circulating Cancer Cells" (2012).
65. UCLA Hawthorne Lectureship, University of California Los Angeles, Los Angeles, CA; "'Artificial Atoms' Formed From Nucleic Acid-Nanoparticle Conjugates" (2012).
66. 22nd Anniversary World Congress on Biosensors (BIOS2012), Cancun, Mexico; "Single Cell Analysis of Intracellular Content with 'Nano-Flares'" (2012).
67. International Workshop on Frontiers of Molecular Science, Beijing, China; "Supramolecular Allosteric Enzyme Mimics - Exceeding the Capabilities of Mother Nature Through Chemistry" (2012).
68. International Workshop on Frontiers of Molecular Science, Beijing, China; "'Artificial Atoms' Formed from Nucleic Acid-Nanoparticle Conjugates" (2012).
69. 5th International Symposium on Bioanalysis, Biomedical Engineering and Nanotechnology (ISBBN), Changsha, China; "Spherical Nucleic Acid (SNA) Nanostructures: Establishing New Paradigms in Materials Synthesis, Molecular Diagnostics, and Intracellular Gene Regulation" (2012).
70. Jawaharlal Nehru Centre for Advanced Scientific Research, ICMS, Bangalore, India; "Artificial Atoms Formed from Nucleic Acid-Nanoparticle Conjugates" (2012).
71. NTU Lee Kuan Yew Visitor Lecture, Singapore; "Nanotechnology: Moving Beyond Small Thinking" (2012).
72. NUS Lee Kuan Yew Visitor Lecture, Singapore; "A Chemist's Approach to Nanofabrication: Towards a 'Desk-Top' Fab" (2012).
73. GRC Drug Carriers Conference, Waterville Valley, NH; "Spherical and Other Three Dimensional Forms of Nucleic Acids: A New and Effective Gene Regulation Platform" (2012).
74. ACS Fall 2012 Plenary Symposium, Philadelphia, PA; "Spherical Nucleic Acid (SNA) Nanostructures: A New Platform for Intracellular Gene Regulation" (2012).
75. ACS Fall 2012 Meeting, Philadelphia, PA; "Artificial Atoms Formed from Nucleic Acid-Nanoparticle Conjugates" (2012).
76. Case Western Reserve University, Allen and Constance Ford Distinguished Lecture Series, Cleveland, OH; "Revolutionizing the Field of Medicine through Advances in Nanotechnology" (2012).

77. University of Rhode Island, Frontiers in Pharmaceutical Sciences Conference, Kingston, RI; "Spherical Nucleic Acid (SNA) Nanostructures: A New Platform for Intracellular Gene Regulation" (2012).
78. Georgia Institute of Technology, Pritchett Lecture, Atlanta, GA; "Nanotechnology: Learning to Think Big in a Field Focused on the Small" (2012).
79. IARPA Workshop, Bedford, MA; "Nanotechnology Platforms for Highly Sensitive and Selective Detection of Biological Markers" (2012).
80. University of Southern California, Ming Hsieh Institute Symposium, Los Angeles, CA; "Research Directions in Nanomedicine for Cancer" (2012).
81. Northwestern University, Shirley Ryan Lecture Series, Chicago, IL; "Revolutionizing the Field of Medicine Through Advances in Nanotechnology" (2012).
82. TecEdge, Wright Brothers Institute Innovation and Collaboration Center, Bio-X Review, Dayton, OH; "Biobarcodes and Nanoflakes: New Nanotechnological Taggant Approaches" (2012).
83. Massachusetts Institute of Technology, MTL Seminar Series, Cambridge, MA; "A Chemist's Approach to Nanofabrication: 'Towards a Desktop Fab'" (2012).
84. Harvard University, Harvard-MIT P-Chem Seminar, Cambridge, MA; "Programmable Atom Equivalents" (2012).
85. Argonne National Laboratory, Joint NSRC Workshop on Nanoparticle Science, Lemont, IL; "Artificial Atoms' Formed from Nucleic Acid-Nanoparticle Conjugates" (2012).
86. TBN Review, Boston, MA; "Scanning Probe Epitaxy" (2012).
87. Nanyang Technological University, Small Sciences Symposium: Frontiers in Nanomedicine, Singapore; "Spherical Nucleic Acid (SNA) Nanostructures: Establishing New Paradigms in Molecular Diagnostics and Intracellular Gene Regulation" (2012).
88. Natural Materials, Systems & Extremophiles Program Review, Washington, DC; "MURI Bioprogrammable 1, 2, 3D Materials" (2013).
89. Natural Materials, Systems & Extremophiles Program Review, Washington, DC; "Nanostructured Interfaces and Patterning Tools for Probing Bioinspired Materials and Systems" (2013).
90. NAS Class Membership Meeting, Irvine, CA; "Single-Cell Analysis of Intracellular Content with 'NanoFlakes'" (2013).
91. ASME NEMB Global Congress on Nanoengineering for Medicine and Biology, Boston, MA; "Single-Cell Analysis of Intracellular Content with 'NanoFlakes'" (2013).
92. AAAS Annual Meeting, Boston, MA; "Convergence of Physical, Engineering, and Life Sciences: Next Innovation Economy" (2013).
93. AAAS Annual Meeting, Boston, MA; "Nucleic Acid-Modified Nanostructures as Programmable Atom Equivalents: Forging a New Periodic Table" (2013).
94. PITTCO Annual Meeting, Philadelphia, PA; "Spherical Nucleic Acid (SNA) Nanostructures: Establishing New Paradigms in Molecular Diagnostics and Intracellular Gene Regulation" (2013).
95. PITTCO Annual Meeting, Philadelphia, PA; "Live Cell Sorting Based on Genetic Content with NanoFlakes" (2013).
96. MRS Spring Meeting, San Francisco, CA; "Programmable Atom Equivalents" (2013).
97. ACS National Meeting, New Orleans, LA; "Programmable Atom Equivalents" (2013).
98. ACS National Meeting, New Orleans, LA; "Controlling the Shape of Silver and Gold Nanostructures with Reaction Kinetics and Surface Chemistry" (2013).

99. Northwestern University, Seeing at the Nanoscale Conference, Evanston, IL; “A Chemist’s Approach to Nanofabrication: Towards a ‘Desktop Fab’” (2013).
100. IVN: Dx Kickoff Meeting, San Diego, CA; “Combating Bacterial Threats with Programmable Bactericides” (2013).
101. IVN: Dx Kickoff Meeting, San Diego, CA; “Spherical Nucleic Acids in In Vivo Therapeutics” (2013).
102. MRS Spring Meeting, San Francisco, CA; “Programmable Atom Equivalents” (2013).
103. GRC Conference, Les Diablerets, Switzerland; “Nucleic Acid-Modified Nanostructures as Programmable Atom Equivalents: Forging a New Periodic Table” (2013).
104. Cambridge University, Lord Lewis Lectureship, Cambridge, UK; “Spherical Nucleic Acid (SNA) Nanostructures: Establishing a New Paradigm in Molecular Diagnostics and Intracellular Gene Regulation” (2013).
105. Cambridge University, Lord Lewis Lectureship, Cambridge, UK; “Nucleic Acid-Modified Nanostructures as Programmable Atom Equivalents: Forging a New Periodic Table” (2013).
106. TIDES Conference, Boston, MA; “Spherical Nucleic Acids (SNAs)” (2013).
107. Honeywell Technology Symposium, Minneapolis, MN; “Nanotechnology: Learning to think big in a field focused on the small” (2013).

Hong

1. S. Hong. US-Korea Workshop on Nanostructured Materials; “Template-directed Assembly Strategies” (2010).
2. S. Hong. PACIFICHEM2010; “Carbon Nanotubes and Nano-Carbon Materials: Preparation Characterization, and Application” (2010).
3. S. Y. Park. Materials Research Society; “Controlled Behavior of Neural Stem Cells on Carbon Nanomaterials” (2010).
4. S. Namgung. Materials Research Society; “Selective Filopodial Extensions of Human Mesenchymal Stem Cells Along Fibronectin-carbon Nanotube Hybrid” (2010).
5. M. Ariff. American Physical Society; “Flexible and Transparent Field Emission Devices based on Graphene-Nanowire Hybrid Structures” (2011).
6. E. Kim, American Physical Society; “Electrical Control of Microtubule Translocation on Graphene” (2011).
7. K.-E. Byun, Biophysical Society Annual Meeting; “Electrochemical Control of Motor Protein Motility Using Conducting Polymer on Graphene for Bio-Inspired Hybrid Nanomechanical Systems” (2011).
8. S. Y. Park. Biophysical Society Annual Meeting; “Enhanced Neural Differentiation of Stem Cells on Carbon Nanomaterials” (2011).
9. S. Hong. US-Korea JSNT2011 “Massively Parallel Nanostructure Assembly Strategies for Sensing and information Technology” (2011).
10. S. Hong. Korean Physical Society; “Graphene as a Transparent Conducting Substrate for Biological Applications: Stem Cell Growth and Protein Assay” (2011).
11. H. J. Jin. Korean Sensor Society; “Artificial Bioelectronic Tongue based on Membrane-Carbon Nanotube (CNT) Hybrid Structures” (2011).
12. S. Hong. 221st ECS Meeting; “Hybrid Nanobio-devices based on Carbon Nanotubes and Nanostructures” (2012).
13. S. Hong. US - Korea Joint Symposium of Nanotechnology Workshop; “Massively Parallel Nanostructure Assembly Strategies for Sensing and Information Technologies”

(2012).

14. S. Hong, SBE's 6th International Conference on Bioengineering and Nanotechnology; "Hybrid Nanobio-Devices based on carbon Nanostructures and biomolecules" (2012).
15. S. Hong. Nano Korea; "Hybrid Nanobio-devices based on Carbon-based Nanostructures" (2012).
16. D. J. Lee. American Physical Society; "Real-Time Control of Biological Motor Activity using Graphene-polymer Hybrid Bioenergy Storage Device" (2013).

e) manuscripts submitted but not yet published, and

None.

f) provide a list any interactions with industry or with Air Force Research Laboratory scientists or significant collaborations that resulted from this work.

- Mirkin gave 18 DoD-related talks
- Mirkin visited several DoD facilities (PI and students), including the AFRL
- Mirkin is collaborating with DoD
- Mirkin brought DoD personnel to campus – for example, Craig Murdock (ARFL), week-long trip (2011)
- Mirkin is engaged in a sponsored research agreement with UOP Honeywell

Attachments: Publications a), b) and c) listed above if possible.

DD882: As a separate document, please complete and sign the inventions disclosure form.